

PAPER • OPEN ACCESS

Polarized fusion and potential *in situ* tests of fuel polarization survival in a tokamak plasma




To cite this article: L. Baylor *et al* 2023 *Nucl. Fusion* **63** 076009

View the [article online](#) for updates and enhancements.

You may also like

- [Vibration analysis of hydrogen, deuterium and tritium in metals: consequences on the isotope effect](#)
Natacha Bourgeois, Jean-Claude Crivello, Pierre Cenedese et al.
- [Isotope effects in lithium hydride and lithium deuteride crystals by molecular dynamics simulations](#)
Hichem Dammak, Ekaterina Antoshchenkova, Marc Hayoun et al.
- [Effect of lattice defects and temperature transition rates on the deuteride \(hydride\) particle morphology and phase transformation thermal hysteresis in niobium](#)
Brent J Heuser and W C Chen

Polarized fusion and potential *in situ* tests of fuel polarization survival in a tokamak plasma

L. Baylor⁶, A. Deur¹ , N. Eidietis² , W.W. Heidbrink^{5,*} , G.L. Jackson², J. Liu³, M.M. Lowry¹, G.W. Miller^{3,4,*}, D. Pace², A.M. Sandorfi^{1,*} , S.P. Smith^{2,*}, S. Tafti³, K. Wei⁷, X. Wei¹ and X. Zheng³

¹ Physics Division, Thomas Jefferson National Accelerator Facility, Newport News, VA 23606, United States of America

² DIII-D National Fusion Facility, General Atomics, San Diego, CA 92186-5608, United States of America

³ Department of Physics, University of Virginia, Charlottesville, VA 22904, United States of America

⁴ Department of Radiology and Medical Imaging, University of Virginia, Charlottesville, VA 22908, United States of America

⁵ Department of Physics and Astronomy, University of California, Irvine, CA 92617, United States of America

⁶ Fusion Energy Division, Oak Ridge National Laboratory, Oak Ridge, TN 37831, United States of America

⁷ Department of Physics, University of Connecticut, Storrs, CT 06269, United States of America

E-mail: heidbrink@fusion.gat.com, gwm2n@virginia.edu, sandorfi@JLab.org and smithsp@fusion.gat.com

Received 9 September 2022, revised 6 March 2023

Accepted for publication 13 March 2023

Published 1 June 2023



Abstract

The use of spin-polarized fusion fuels would provide a significant boost towards the ignition of a burning plasma. The cross section for $D + T \rightarrow \alpha + n$, would be increased by 1.5 if the fuels were injected with parallel polarization. Furthermore, our simulations demonstrate additional non-linear power gains in large-scale machines such as ITER, due to increased alpha heating. Such benefits require the survival of spin polarizations for periods comparable to the particle confinement time. During the 1980s, calculations predicted that polarizations could survive a plasma environment, although concerns persisted regarding the cumulative impacts of wall recycling. In that era, technical challenges prevented direct tests and left the large scale fueling of a power reactor beyond reach. Over the last decades, this situation has changed dramatically. Detailed simulations of ITER have predicted negligible wall recycling in a high-power reactor, and recent advances in laser-driven sources project the capability of producing large quantities of $\sim 100\%$ polarized D and T. The remaining crucial step is an *in-situ* demonstration of polarization survival in a plasma. For this, we outline a measurement strategy using the isospin-mirror reaction, $D + {}^3\text{He} \rightarrow \alpha + p$. Polarized ${}^3\text{He}$ avoids the complexities of handling tritium, while encompassing the same spin-physics. We evaluate two methods of delivering deuterium, using dynamically polarized Lithium-Deuteride (with vector polarization P_V^D of 70%) or frozen-spin Hydrogen-Deuteride (with P_V^D of 40%), together with a method of

* Authors to whom any correspondence should be addressed.



Original content from this work may be used under the terms of the [Creative Commons Attribution 4.0 licence](https://creativecommons.org/licenses/by/4.0/). Any further distribution of this work must maintain attribution to the author(s) and the title of the work, journal citation and DOI.

injecting optically-pumped ^3He (with 65% polarization). Pellets of these materials all have long polarization decay times (~ 6 min for LiD at 2 K, ~ 2 months for HD at 2 K, and ~ 3 d for ^3He at 77 K), all far greater than a plasma shot in a research tokamak such as DIII-D (~ 20 s). Both species can be propelled from a single cryogenic injection gun. We review plasma requirements and strategies for detecting polarization survival. Polarization alters both fusion yields and the angular distribution of fusion products, and each of these provides a potential signal. In this paper we simulate a selection of shots with similar characteristics in a future high- T_{ion} H plasma, and find ratios of yields from shots with fuel spins parallel and antiparallel reaching 1.3 (HD + ^3He) to 1.6 (LiD + ^3He) over a wide range of poloidal angles. (A companion paper finds sensitivity to fusion product angular distributions as reflected in the pitch angles of protons and alphas reaching the plasma facing wall.)

Keywords: polarization-survival, pellet-fueling, fuel-polarization, alpha-heating

(Some figures may appear in colour only in the online journal)

1. Introduction

The primary nuclear reaction for both magnetic and Inertial Confinement Fusion (ICF) machines is $\text{D} + \text{T} \rightarrow \alpha + \text{n}$. Both this reaction and its isospin-mirror process, $\text{D} + ^3\text{He} \rightarrow \alpha + \text{p}$, are dominated at low energies by spin $3/2$ fusion resonances that are just above the particle-decay thresholds in the compound nuclei ^5He and ^5Li , respectively [1, 2]. At keV energies such reactions are dominated by s -wave processes without any entrance-channel orbital angular momentum. Under these conditions it is obvious that a spin 1 deuteron and a spin $1/2$ triton (or ^3He) will preferentially fuse into a spin $3/2$ state when their spins are parallel, so an alignment of their spins would lead to an enhancement of the reaction cross section. While this had been known for decades [3], spin alignments are usually associated with low temperatures and the possibility that they could survive in a 10^8 kelvin plasma for long enough to be useful seemed counter-intuitive. A paradigm shift came in 1982 with the seminal work of Kulsrud, Furth, Valeo and Goldhaber [4], which predicted time scales for polarization loss in a plasma that were much longer than the characteristic fuel burn-up period. Since polarization-enhanced cross sections could potentially increase fusion efficiency (by $\sim 50\%$, as discussed in section 2), that paper led to considerable theoretical activity over the subsequent decade—[5–10] and references therein.

During this period of initial excitement, a favorable cost-benefit estimate was carried out [11, 12], assuming general projections regarding the possible cost of polarizing fuel (which in the light of subsequent developments are probably pessimistic [13]). Several polarization methods and many possible depolarization mechanisms were assessed, [6–10]. However, polarized nuclei were only available as gases or atomic beams of too low intensity to produce an observable signal, or as complex molecules containing high Z species whose large ionization energies would readily quench any plasma. In addition, there was no efficient means to deliver polarized fuel into a plasma, and so no practical way of testing the predictions of polarization survival. In that era, a burning plasma seemed well within reach, and the research needed to overcome the obstacles associated with polarized fuel seemed too much effort for too little gain. As a result, no experimental test

was ever carried out and research activity in this area all but died out.

Over the last 30 years, igniting a plasma has turned out to be much more difficult than had been anticipated and increasing the reactivity by a factor of 1.5 (and the Q of a power reactor by 1.8, as discussed in section 3) now seems quite attractive, even if only as a safety net against future challenges. Over the same period, there have been key advances in the production of highly-polarized H and D, driven by Nuclear and Particle Physics (NP) experiments [14–16], as well as in the production of hyper-polarized ^3He gas for use both as a contrast agent in medical imaging [17–19] and in high-energy spin physics. ICF polymer shell technology has also been developed [20], and can now be used to contain polarized fuel (section 5). Finally, cryogenic injection guns have been demonstrated to convey pellets into the core of tokamak plasmas with high efficiencies [21]. The combination of these technologies that have matured since the original Kulsrud *et al* paper [4] can now be used to test the long-standing prediction of polarization survival, using the $\text{D} + ^3\text{He} \rightarrow \alpha + \text{p}$ reaction [13, 22]. As discussed below (section 2), the ^5He and ^5Li compound states in the $\text{D} + \text{T} \rightarrow \alpha + \text{n}$ and $\text{D} + ^3\text{He} \rightarrow \alpha + \text{p}$ reactions have a nearly identical low-energy structure. Thus, polarization experiments can be conducted using the $\text{D} + ^3\text{He} \rightarrow \alpha + \text{p}$ process, and the lessons learned directly applied to the planning of polarized $\text{D} + \text{T} \rightarrow \alpha + \text{n}$. (We note that while one might also consider polarized $\text{D} + \text{D}$ reactions for such a test, the nuclear processes involved are in fact much more complicated. Current theoretical predictions for reaction rates with parallel deuteron spins span the range from a suppression by a factor of 10 to an enhancement of 2.5 over the unpolarized case [23]. Direct measurements at the low energies relevant to tokamak plasmas is very challenging. A program to detect low-energy polarized $\text{D} + \text{D}$ reactions is under development [24], although as yet no results are available. Thus, while a study of polarized $\text{D} + \text{D}$ has interesting nuclear structure ramifications, its use for quantifying polarization survival in a plasma presents many complications.)

Polarization survival is a key question, and in this paper we detail how an experimental test can be executed. The goals of the research that have led to the advances in polarized

materials during the last decades, few mole samples with 10^5 – 10^8 s lifetimes, are very mismatched to the requirements of fusion energy where ultimately several kilo-moles per day would be needed, but with merely few second polarization lifetimes. Nonetheless, current technologies and existing facilities can be exploited in a cost-effective way for a test of polarization survival [25]. While new laser-driven methods project the capability of feeding a reactor with polarized fuel (as discussed briefly in section 5.3 and appendix D), the crucial question of polarization survival must be addressed before investing in the development effort.

We continue with a review in the next section of the polarization-dependent reaction cross sections. In section 3 we report simulations of the additional impacts of polarized fuel from alpha heating in a large-scale tokamak, such as ITER. In section 4 we summarize expectations for depolarization rates from various possible loss mechanisms. The rest of the paper is devoted to a detailed study of a viable polarization-survival test experiment using two sets of pellets, one containing a solid form of polarized deuterium (and two options are considered) and the other polarized ^3He gas, both introduced into the plasma of a tokamak by pellet injection. Fuel preparation considerations are discussed in section 5. Plasma requirements, including the need for the development of a high- T_{ion} H plasma, and detection strategies for a polarization survival experiment are summarized in section 6 for the particular example of the DIII-D tokamak. Section 6 continues with a simulation of projected polarization-dependent changes in the fusion product yields reaching the plasma-facing walls. (A companion paper simulates a polarization life-time experiment through measurements of changes in fusion angular distributions, as reflected in the pitch angles of fusion products reaching the outer walls [26].)

This paper outlines an experiment that cannot be executed without active participation from three very different disciplines—Fusion Energy Sciences, NP, and Radiological Imaging. Various details are included that may appear redundant to one group or another, but are included here for the sake of the broader audience. General concepts and preliminary progress on some aspects of this work have been reported in [13, 22, 25, 27, 28].

2. Polarization-dependent fusion reactions

The polarization dependences and angular distributions of fusion cross sections are determined by the contributing levels in the fused compound nucleus. (Direct p/n stripping and pickup reactions are completely insignificant at tokamak energies.) If only a single compound state contributes, polarization enhancements will be entirely determined by angular momentum and parity conservation. However, interfering transitions through neighboring levels could in principle complicate the problem. To address the magnitude of such effects we first consider the relevant energy range.

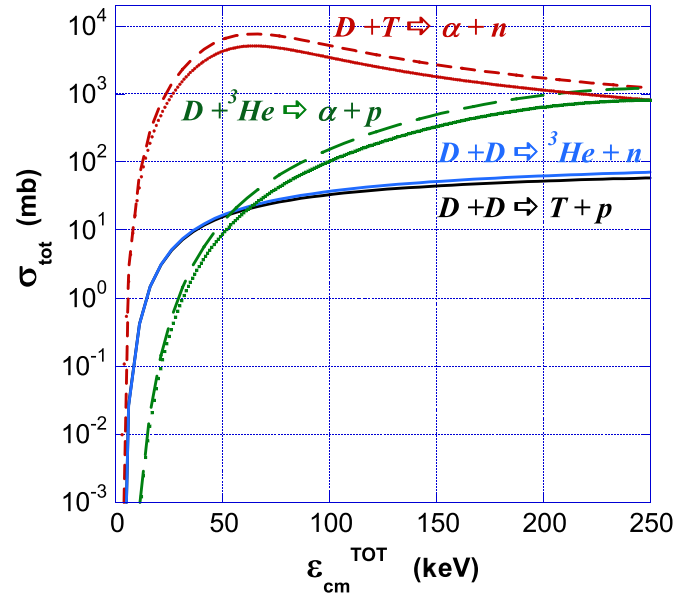


Figure 1. Total cross sections for relevant fusion reactions, evaluated using [29]. Dashed curves reflect a polarization-enhancement factor of 1.5. (Possible polarization effects on D + D reactions are not shown because of their large uncertainty).

2.1. Fusion states at tokamak energies

Angle-integrated cross sections for the main fusion processes are shown in figure 1 as a function of their total Center of Mass (CM) kinetic energy [29], assuming no polarization in the entrance channels. While the $\text{D} + \text{T} \rightarrow \alpha + \text{n}$ and $\text{D} + ^3\text{He} \rightarrow \alpha + \text{p}$ reactions become comparable above 250 keV, the former completely dominates at low energies. D + D reactions are intermediate at low energies but drop below other channels above 65 keV. A thermonuclear plasma contains a distribution of energies and the net fusion rate of two species are determined by their densities, N_1 (cm^{-3}) and N_2 (cm^{-3}), the effective plasma volume V (cm^3), and the cross section averaged over a Maxwell-Boltzmann velocity distribution $\langle \sigma v \rangle$ ($\text{cm}^3 \text{s}^{-1}$) [30],

$$\langle \sigma v \rangle = \frac{4c}{\sqrt{2\pi M_r} (k_B T)^{3/2}} \int e^{-\varepsilon/k_B T} \varepsilon \sigma(\varepsilon) d\varepsilon. \quad (1)$$

Here, ε is the total CM kinetic energy of the thermonuclear reaction, $M_r = m_1 m_2 / (m_1 + m_2)$ is the reduced mass and $k_B T$ is the ion temperature expressed in keV using Boltzmann's constant. (This assumes thermal distributions. When plasmas are heated with the injection of neutral beams, e.g. ~ 80 keV at DIII-D, an additional rate component comes from the beam-plasma interactions at the higher CM energy.) The fusion rates of equation (1) determine the relevant energy ranges for the various channels. The $\langle \sigma v \rangle$ integrals, running as a function of the upper limit of integration, are essentially saturated by about 50 keV for D + T, and by about 100 keV for D + ^3He [13].

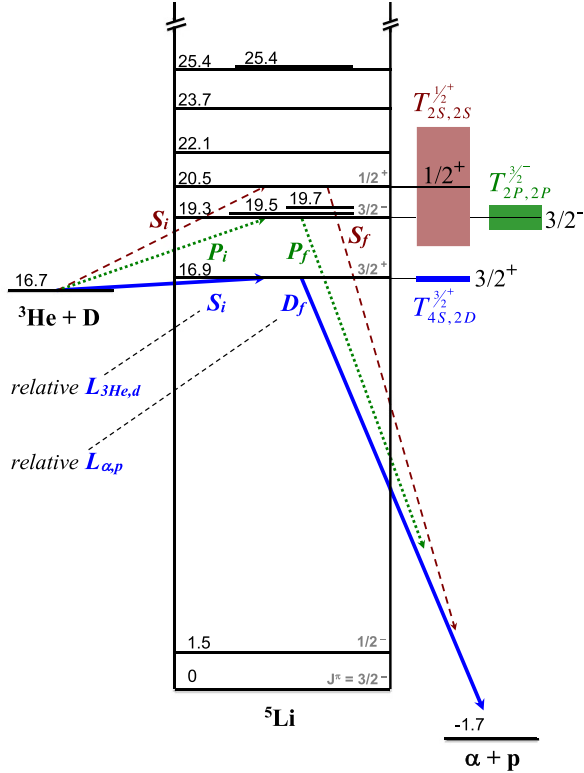


Figure 2. The energy level spectrum of ${}^5\text{Li}$, with energies from [31]. The widths of spin 1/2 and 3/2 states are schematically represented by the adjacent vertical bars. The orbital angular momenta in the entrance and exit channel of the $\text{D} + {}^3\text{He} \rightarrow \alpha + \text{p}$ reaction are indicated.

The ${}^5\text{He}$ and ${}^5\text{Li}$ compound states in the $\text{D} + \text{T} \rightarrow \alpha + \text{n}$ and $\text{D} + {}^3\text{He} \rightarrow \alpha + \text{p}$ reactions are isospin-mirror nuclei and have a nearly identical low-energy structure. Both have a spin 3/2 capture resonance just above their particle decay thresholds, at 16.84 MeV in ${}^5\text{He}$ (50 keV above the $\text{D} + \text{T}$ threshold) and at 16.87 MeV in ${}^5\text{Li}$ (210 keV above the $\text{D} + {}^3\text{He}$ threshold) [31]. Both compound nuclei have a gap of over 2.3 MeV between this $J = 3/2$ fusion resonance and the next excited level, so that the only possible way higher states can contribute to fusion at tokamak energies is through the low-energy tails of broad states. Of the two reactions, $\text{D} + {}^3\text{He} \rightarrow \alpha + \text{p}$ has the greater potential for encountering effects from interfering intermediate states, because of the higher energy of its spin 3/2 fusion resonance in ${}^5\text{Li}$ and the higher reach of its $\langle \sigma v \rangle$ integral.

The level spectrum of ${}^5\text{Li}$ is shown in figure 2 [31]. The spin 3/2 second excited state at 16.9 MeV is the intermediate state of the ${}^3\text{He} + \text{D}$ fusion resonance. For fusion through this compound state, angular momentum and parity conservation limit the orbital angular momentum to $L_i = 0$ (S-wave) in the entrance channel, and to $L_f = 2$ (D-wave) in the $\alpha + \text{p}$ final state. We follow the notation of Hale [32, 33] and of Lane and Thomas [34] and designate this transition amplitude as $T_{(2S_i+1)L_i, (2S_f+1)L_f}^{J^\pi} = T_{4S, 2D}^{3/2+}$. Fusion through higher spin states

requires larger orbital angular momenta, which are greatly suppressed at tokamak plasma energies. There are only two other low-spin levels that might conceivably contribute, due to their very large widths, a $J^\pi = 3/2^-$ state at 19.3 MeV above the ground state with a width of 1 MeV and a $1/2^+$ level at 20.5 MeV that has a 5 MeV width [31]. The corresponding transition amplitudes are designated $T_{2P, 2P}^{3/2-}$ and $T_{2S, 2S}^{1/2+}$, respectively. In this convention, the S -matrix is just $2i \cdot T$, and the total unpolarized cross section, averaged over initial spin states and summed over final ones, is

$$\sigma_0 = \frac{4\pi}{(k_D^{cm})^2} \sum \frac{(2J_{Li} + 1)}{(2J_D + 1)(2J_{He} + 1)} \left| T_{(2S_i+1)L_i, (2S_f+1)L_f}^{J^\pi} \right|^2. \quad (2)$$

Here the leading factor $k_D^{cm} = P_D/\hbar$ is the deuteron wave-number (and P_D its momentum) in the CM.

An R -matrix analysis [35], fitting all recent polarization data, has been used to determine the transition amplitudes shown in the upper panel of figure 3. In this energy range, the $T_{4S, 2D}^{3/2+}$ amplitude for transitions through the $J^\pi = 3/2^+$ fusion resonance always dominates by more than an order of magnitude. The leading interference terms with the $T_{2P, 2P}^{3/2-}$ and $T_{2S, 2S}^{1/2+}$ transitions are plotted in the lower panel as the solid and dashed curves, respectively. (All other interference terms are at least an order of magnitude smaller.) For completeness, we have also plotted as a dotted curve the combination of amplitudes that determines the factor f considered by Kulsrud and collaborators [4]; $1 - f$ is plotted in figure 3 since f is negligibly different from unity at all energies.

While recent polarization experiments have strongly affected the evaluation of the weaker transition amplitudes, there has been no real change to the total cross section, in which all interference terms drop out. A calculation of the total cross section with equation (2) and the amplitudes of figure 3 is indistinguishable from the 1992 evaluation of Bosch and Hale [29] that is plotted in figure 1.

2.2. Angular dependence in spin 1/2 + spin 1 polarized reactions

The general formalism for calculating decay angular distributions in the $\text{D} + ({}^3\text{He}/\text{T}) \rightarrow \alpha + (\text{p}/\text{n})$ reactions with a fully polarized entrance channel have been discussed in the literature for various intermediate-state spins [36–40]. These follow from angular momentum and parity considerations. (As an illustration, a simple derivation for fusion from parallel and anti-parallel initial-state spin alignments is given in appendix A). In terms of the contributing amplitudes of figure 3, the final state cross section can be written as,

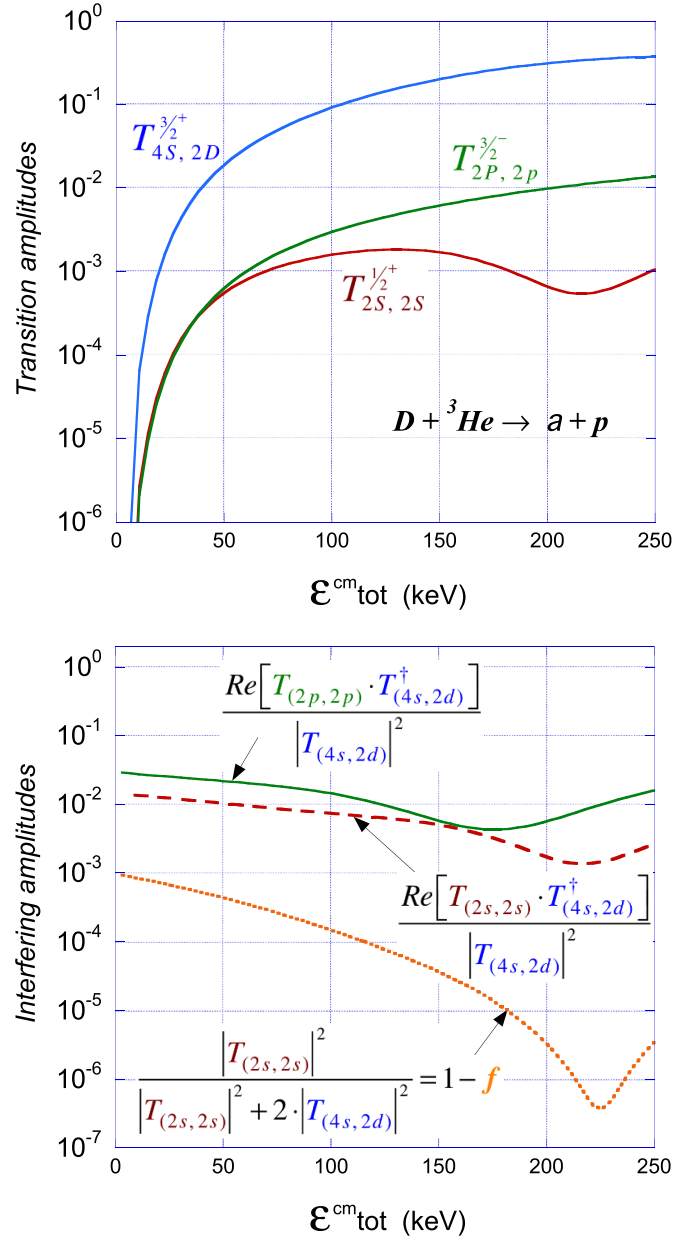


Figure 3. Transition amplitudes (dimensionless) for the $D + {}^3\text{He} \rightarrow \alpha + p$ reaction, determined from a recent R -matrix fit to all data up to 2006 [35] are shown in the upper panel. The leading terms contributing to the cross section from interference between the $T_{(4s,2d)}$ amplitude through the dominant $3/2^+$ compound state and $T_{(2p,2p)}$ and $T_{(2s,2s)}$ transitions through $3/2^-$ and $1/2^+$ states are plotted in the lower panel as solid and dashed curves, respectively. The dotted curve shows the dependence of $(1 - f)$, where f is the only interference term discussed in [4].

$$\frac{d\sigma}{d\Omega_{cm}} = \left(\frac{d\sigma}{d\Omega} \right)_0 \left\{ \begin{aligned} &1 - \frac{1}{2} P_D^Y P_{3\text{He}}^Y [1 + (1 - f)] \\ &+ \frac{1}{2} [1 - (1 - f)] \cdot \left[3 P_D^Y P_{3\text{He}}^Y \sin^2 \theta + \frac{1}{2} P_D^T (1 - 3 \cos^2 \theta) \right] \\ &- \frac{\text{Re} \left({}^{1/2+} T_{2s,2s} {}^{3/2+} T_{4s,2d}^\dagger \right)}{|{}^{3/2+} T_{4s,2d}|^2} (P_D^Y P_{3\text{He}}^Y - P_D^T) (1 - 3 \cos^2 \theta) + \dots \end{aligned} \right\}. \quad (3a)$$

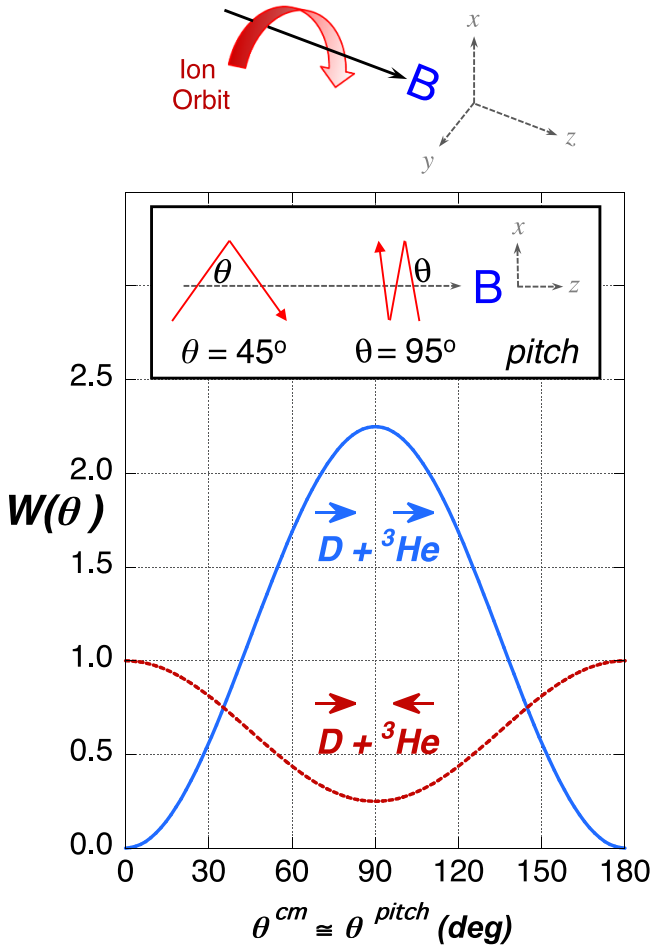


Figure 4. Ions follow helical paths around the local magnetic field lines. The *pitch* (polar) angles θ of reaction products are measured relative to the local field direction, as indicated schematically at the top of the figure. In the lower graph the angular distribution function $W(\theta)$ from equation (4) has been evaluated for full vector polarization: $|\mathbf{P}_D^V| = 1$, $\mathbf{P}_D^T = 1$, and $|\mathbf{P}_{He}| = 1$. The solid (blue) curve assumes parallel D and ${}^3\text{He}$ spins, while the dotted (red) curve is calculated for anti-parallel spin alignment. Adapted from [13], with permission from Springer Nature. (A simple derivation of these distributions is given in appendix A).

Here the leading factor $(d\sigma/d\Omega)_0 = \frac{1}{4\pi}\sigma_0$ is the isotropic distribution determined by equation (2) that would be observed in the absence of initial-state polarization. The factor $P_{He} = N_{+1/2} - N_{-1/2} \in [-1, +1]$ is the degree of ${}^3\text{He}$ polarization, determined by the sub-state population fractions relative to the tokamak magnetic field direction. Similarly, $P_D^V = (N_{+1} - N_{-1}) \in [-1, +1]$ is the deuteron vector polarization and $P_D^T = (N_{+1} + N_{-1} - 2N_0) \in [-2, +1]$ is the associated deuteron tensor polarization. The pitch (polar) angle θ is measured relative to the local magnetic field, as shown schematically at the top of figure 4. The leading interference terms all appear as the real part of products of weaker amplitudes with the dominant $T_{4S,2D}^{3/2+}$; one such term is shown explicitly in equation (3a) as an example. For completeness, equation (3b) also includes the

combination of interfering amplitudes considered by Kulsrud et al [4],

$$f = \frac{2|^{3/2+}T_{4S,2D}|^2}{|^{1/2+}T_{2S,2S}|^2 + 2|^{3/2+}T_{4S,2D}|^2}. \quad (3b)$$

As seen in the lower panel of figure 3, the leading interference terms provide less than a 3% correction to the angular distribution even at the lowest energies, and the $(I - f)$ factor that enters the cross section is completely negligible at all energies. Thus, to an excellent approximation the differential cross section for the $D + {}^3\text{He} \rightarrow \alpha + p$ reaction, as well as for $D + t \rightarrow \alpha + n$ (with P_t replacing P_{He}) where the interference terms are even smaller, may be simplified to,

$$\frac{d\sigma}{d\Omega_{cm}} = \left(\frac{d\sigma}{d\Omega}\right)_0 \left\{ 1 - \frac{1}{2}P_D^V P_{He} + \frac{1}{2} \left[3P_D^V P_{He} \sin^2\theta + \frac{1}{2}P_D^T (1 - 3\cos^2\theta) \right] \right\}, \quad (4a)$$

and the Maxwell-averaged cross section becomes,

$$\langle d\sigma(\theta)\nu \rangle = \frac{1}{4\pi} \langle \sigma_o \nu \rangle \cdot W(\theta) = \frac{1}{4\pi} \langle \sigma_o \nu \rangle \cdot \left\{ 1 - \frac{1}{2}P_D^V P_{He} + \frac{1}{2} \left[3P_D^V P_{He} \sin^2\theta + \frac{1}{2}P_D^T (1 - 3\cos^2\theta) \right] \right\}. \quad (4b)$$

Several observations are worth noting about the structure of equation (4). The simple factorization in equation (4b) holds as long as we neglect the interference terms, which as we have seen is an excellent approximation. If the ${}^3\text{He}$ is unpolarized, the angular dependence of the differential cross section is modified from isotropy only by the tensor polarization of the deuteron. However, the angular factor of that term, $(1 - 3\cos^2\theta)$, integrates to zero in the total cross section so that the total reaction rate is not modified. (Nonetheless, as discussed in [10, 25], this could potentially provide a measure of control over the direction of neutrons from $D + T$.) If the deuteron is unpolarized, the angular function $W(\theta)$ reduces to unity. Thus, the total fusion reaction rate differs from the unpolarized case only if *both* reacting species are polarized.

The angular distributions calculated from equation (4) for full vector polarization $\{|\mathbf{P}_D^V| = 1, \mathbf{P}_D^T = 1, \text{ and } |\mathbf{P}_{He}| = 1\}$ are plotted in figure 4. For the case where the D and ${}^3\text{He}$ (or T) spins are both parallel to the magnetic field, the angular function of equation (4), $W(\theta)$, reduces to $9/4 \cdot \sin^2\theta$, which is plotted as the solid (blue) curve; for the corresponding case of anti-parallel spin alignment, $\{P_D^V = \pm 1, P_D^T = 1, \text{ and } P_{He} = \mp 1\}$, $W(\theta)$ becomes $1/4 \cdot (1 + 3\cos^2\theta)$ which is shown as the dotted (red) curve. These are the polarization-dependent fusion-product distributions in a plane perpendicular to the local field. The full three-dimensional distribution of particles is obtained by rotating this plane around the local field direction through the full 360° range of gyro-phase (azimuthal) angles. (In a D + T reactor, running with parallel polarization

would increase the neutron loading on the inner wall, although only from a relatively small fraction of the gyro-phase space. Nonetheless, this is worth considering when designing reactor cooling.)

The enhancement from parallel spin alignment is obvious in figure 4. Integrating equation (4) over all pitch (θ) and gyro-phase (ϕ) angles, determines the total reaction rate as,

$$\langle\sigma\nu\rangle = \langle\sigma_0\nu\rangle \left\{ 1 + \frac{1}{2} \vec{P}_D^V \cdot \vec{P}_{^3\text{He}} \right\}, \quad (5)$$

where here we write the polarization factors as vectors, reflecting their range between $[-1, 1]$. Thus, if the spins of the reacting species are anti-parallel, the reaction rate is 1/2 of the unpolarized rate. But if the initial spins are parallel, the reaction rate is enhanced by a factor of 3/2, which is the original observation of Kulsrud [4].

3. Potential impacts for large-scale tokamaks

The fields and dimensions of high-power tokamaks such as ITER are designed to confine the alpha fusion products. Coulomb interactions of these alphas with electrons and with fuel ions raise the plasma temperature. At the expected ITER plasma temperatures, $k_B T_{\text{ion}}$, of 10–20 keV [41], $\langle\sigma\nu\rangle$ increases roughly as the ion temperature squared. This leads to an additional non-linear increase in the fusion power with polarized fuels beyond the simple polarization factors of equation (5).

3.1. Steady-state power enhancement from polarized reactions

To project the equilibrium power output of an ITER-scale reactor fueled with polarized D and T we have solved the heat diffusion equation for the plasma temperature T ,

$$\frac{\partial T}{\partial t} + \nabla \cdot \Gamma = S. \quad (6)$$

Here, Γ is the heat flux density (related to $-\nabla T$) and S represents the *sources* (or *sinks*) of energy, $S = S_\alpha + S_{\text{aux}} + S_{\text{rad}}$, where $S_\alpha = n_D n_T \cdot \langle\sigma(T)\nu\rangle \cdot E_\alpha \cdot F$ represents the source from fusion reactions, with $F \in [1.0, 1.5]$ included here as a polarization enhancement factor, so that $F = 1.5$ corresponds to the fully polarized limit of equation (5). The parameter S_{aux} represents the external auxiliary heat applied to the plasma, and S_{rad} represents the heat lost from the plasma due to radiation. The code *TRANSP* [42] has been used to model the distributions of S_{aux} and S_{rad} . The heat flux perpendicular to the magnetic field lines arises from the helical motion of confined particles, smeared by coulomb scattering from electrons and ions (*classical transport*). Trapped particles experience a curvature drift with a coulomb smearing comparable to the dimensions of confined orbits (*neoclassical transport*), which is generally much larger [43, 44]. Larger still is the effect of *turbulence*, driven by electron and ion temperature and density gradients. In our simulations, the heat flux density has

been taken as the sum of Γ (*neoclassical* and *classical*) + Γ (*turbulence*). For a steady-state condition, the heat flux must be matched to the source,

$$\Gamma_{\text{neo}} + \Gamma_{\text{turb}} = \int S dV. \quad (7)$$

The calculation has been carried out for the ITER plasma, using the code NEO [45] to capture the effects of neoclassical and classical transport by numerically solving the drift-kinetic equation [46]. Turbulent flow has been simulated in a *trapped gyro-Landau-fluid* model using the code *TGLF* [47]. The steady-state condition of equation (7) for ITER was obtained with the code TGYRO [48]. In the TGYRO simulations the electron density, electron temperature, and thermal ion temperatures were evolved. As the electron density was evolved, the D and T density profiles were scaled to maintain the same ratio to the electron density as the initial ratios. An ITER D + T hybrid H-mode plasma [49], with a ratio of fusion power to injected auxiliary power of $Q = 12$ (including a safety factor $q_{\text{min}} \sim 1.5$ at a plasma radius $\rho = 0.3$) was used with 40 MW of externally supplied auxiliary power (P_{aux}) as the $F = 1$ starting point. (The $Q = 12$ case here contains the typical $Q = 10$ scenario sources, but the TGYRO solution predicts $Q = 12$.) The core electron density in this reference model plasma was $\sim 1.3 \times 10^{20} \text{ m}^{-3}$, accompanied by 100 MW of power in fusion alphas (P_α), so that $Q_\alpha = P_\alpha / P_{\text{aux}} = 2.5$ without fuel polarization. (The total fusion power will be $5 \times P_\alpha$.) The resulting thermal ion and electron temperatures and densities in the plasma core are plotted in figure 5, as a function of the polarization enhancement factor F .

The predicted steady-state power from α heating transferred to ions and electrons is plotted in the top panel of figure 6. (A condensed summary of these simulations is given in [28].) The sum of ion and electron contributions reflects the total alpha power. The associated power in fusion neutrons from $\text{D} + \text{T} \rightarrow \alpha + n$ is four times higher, and the total reactor power is five times the *total* values (diamond points) in figure 6. The lines below the points show the expected result from just the polarization enhancement to the cross section of equation (5). The excess reflects the increased alpha heating, which effectively shifts the CM reaction energy to a higher temperature where the cross section is larger. In this steady-state condition, the net effect of fully polarized fuel ($F = 1.5$) would be an increase in the fusion power by a factor of 1.8. This substantial enhancement is reflected in Q , the fusion energy gain factor (the ratio of the fusion power to the auxiliary heating), as shown in the bottom panel of figure 6. In these simulations, an increased fusion rate with simultaneous increases in densities implies that the plasma is transporting fuel from the edge to the core. The required edge fueling has not been self-consistently modeled—the pedestal region where the fueling would occur is held fixed in these simulations. It is unknown whether the edge fueling would cool the pedestal more than the pedestal would be heated by evolving the pedestal self-consistently—the increased core pressures at higher cross section factor should lead to higher pedestal pressures.

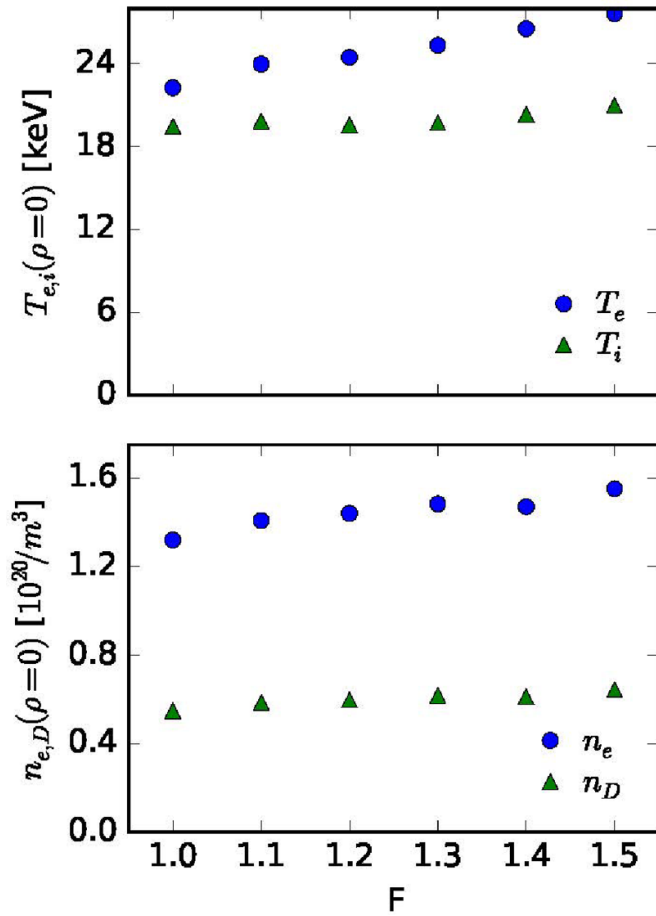


Figure 5. Expected core temperatures (top panel) and densities (bottom panel) of ions (triangles) and electrons (circles) for a steady-state condition in an ITER scale reactor, plotted for different values of the polarization enhancement factor $1.0 \leq F \leq 1.5$.

3.2. Implications for magnetic fields in high power reactors

The fusion rate is the product of $\langle\sigma v\rangle$ with the fuel densities and the plasma volume, peaking in the core where the magnetic field is highest. (For example, see figures 7 and 15 in the subsequent sections.) The option of increasing $\langle\sigma v\rangle$ with polarized fuel could meet the same power goal with a reduced magnetic field. This opens the possibility of using fuel polarization to compensate for field degradation of superconducting coils in existing machines. For future tokamaks, since plant costs scale roughly with the square of the field \times volume product, fuel polarization could potentially be used to optimize construction costs.

4. Depolarization mechanisms in large and research-scale tokamaks

To be useful fuel polarization must survive, first as the polarized species undergo ionization, and then while they circulate as ions in the plasma. The impact of depolarization mechanisms in a large-scale (e.g. ITER) machine versus a research tokamak can be very different.

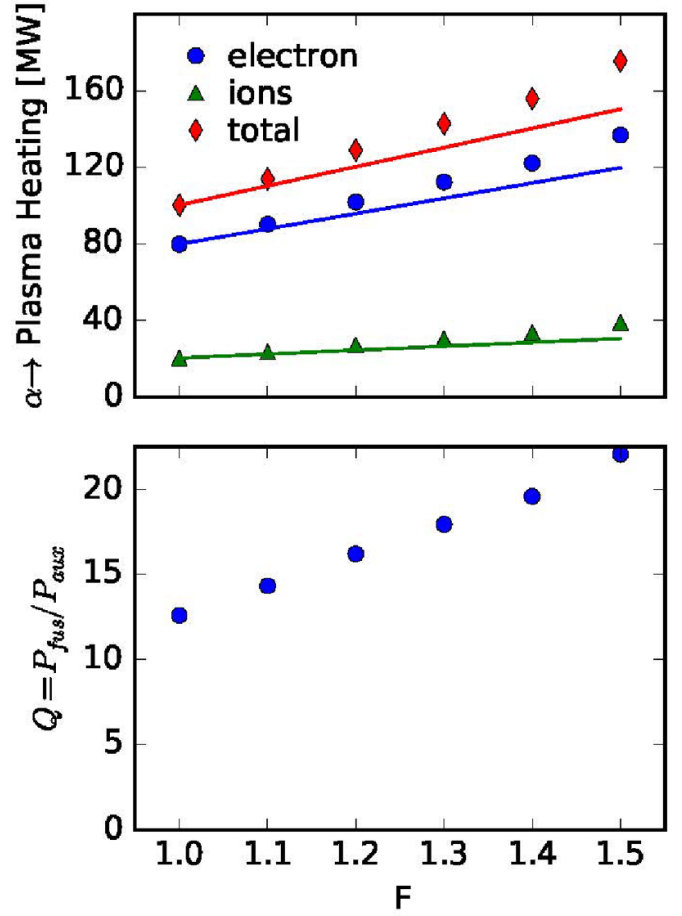


Figure 6. Predicted steady-state fusion heating levels in ions (triangles), electrons (circles) and their sum (diamonds), top panel, for increasing values of the polarization enhancement factor $1.0 \leq F \leq 1.5$. Lines show the expected behavior without alpha heating. The sum *total* reflects the power in fusion alphas. The ratio of fusion power (α + neutrons) to the 40 MW of auxiliary heating (P_{aux}) is plotted in the lower panel.

4.1. Dilution from hyperfine splitting in partially ionized states following injection

The neutral ground states of all potential fusion fuels, either molecular TD or HD , as well as D_2 or T_2 , or atomic 3He , include two electrons paired in a zero-spin 1s state having no net interaction with their nuclei. Upon injection, the nuclear spins immediately align along the local field. The magnetic field direction and magnitude changes are slow with respect to the nuclear precession frequency, which is the same order of magnitude as the cyclotron frequency, and hence adiabatic. A collision with circulating plasma electrons will quickly strip away the first atomic/molecular electron, and then the second on a time scale of $\sim 10 \mu s$ later, which is still much longer than the precession time. In the interval before the nuclei are fully stripped and one electron is still bound, a Hyperfine Interaction (HFI) with the remaining bound electron will occur. As a consequence, the system eigenstates will no longer be pure Zeeman states, and this will result in a degree of dilution of the nuclear polarization. This interaction scales roughly with the cube of the nuclear charge, so the resulting dilution will

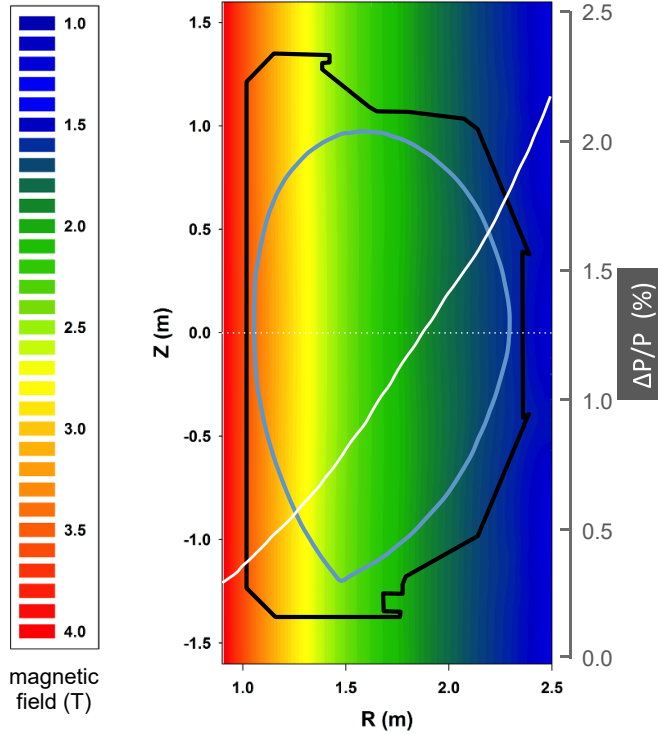


Figure 7. The magnitude of the DIII-D magnetic field in shot 96369 at $t = 4575$ ms, 25 ms after pellet injection, is plotted in color contours with the scale legend to the left. The black polygon shows the relative position of the DIII-D vacuum chamber. The blue teardrop indicates the boundary of the last closed field line. The white curve, with its scale on the right, shows the fractional loss in ^3He polarization along the $Z = 0$ mid-plane, due to hyperfine mixing in partially ionized $^3\text{He}^+$.

be largest for ^3He . We discuss this issue here since, to the best of our knowledge, it has not been treated elsewhere. The calculation for ^3He is outlined in appendix B. The net fractional polarization loss as a function of magnetic field reduces to,

$$\frac{\Delta P}{P} = \frac{1}{2} \left[1 + \frac{4(\mu_e - \mu_{\text{ion}})^2}{A_{\text{HFI}}^2} B^2 \right]^{-1}, \quad (8)$$

where the magnetic moments of the spin $1/2$ electron and ^3He are $\mu_e = (1/2)\gamma_e/2\pi = -14.013$ GHz/tesla [50] and $\mu_{\text{ion}} = (1/2)\gamma_{^3\text{He}}/2\pi = -0.016$ GHz/tesla [51], respectively. In ^3He where the HFI strength (the level splitting in the zero-field limit) is $A_{\text{HFI}} = -8.66565$ GHz (table 1), this results in 2% polarization loss at a field of 1.5 tesla. In a high field tokamak such as ITER, this effect will clearly be negligible. But for research-scale machines such as DIII-D a more careful estimate is necessary.

The magnetic fields in a tokamak are chiefly determined by the torus coils, where fields fall radially with $1/R$. But the fields are modified by the poloidal coils and the plasma current itself. At DIII-D, the fields are obtained by solving the *Grad-Shafranov* equations for Magneto-Hydrodynamic equilibria to determine the plasma current, using as constraints external

magnetic field measurements and coil currents, together with current profiles from a number of diagnostics [52]. The magnitude of the DIII-D field in D_2 pellet shot S-96369 is plotted in figure 7. An illustration of hyperfine mixing effects in such fields is shown as the white curve, which gives the fractional loss in ^3He polarization calculated from equation (8), assuming the magnetic fields along the $Z = 0$ mid-plane. There the polarization loss ranges from 0.4% to 1.7%. The net effective polarization reduction must be weighted by the ^3He density in different field regions.

The expected density profile from the injection of a ^3He pellet has been modeled from measurements of shot S-96369, in which a D_2 pellet was injected into a deuterium plasma. The temperature and density of plasma electrons just prior to pellet injection is shown in the left panel of figure 8. These determine the pellet deposition profile. An impurity level of fully-stripped carbon is also present (from the DIII-D graphite walls), and its density distribution is monitored with a *Charge-Exchange-Recombination* diagnostic [53]. A *Thompson Scattering* diagnostic [54] is used to monitor the electron density profile. Charge balance, $6N(\text{C}6^+) + N(\text{D}) = N(e)$, then determines the deuterium density (which includes deuterons injected as neutral beams). The difference in $N(\text{D})$ before and after the pellet injection is taken as representing the contribution of a pellet. The resulting distribution shown in the right panel of figure 8 is assumed for a ^3He pellet injection.

The mean polarization loss from hyperfine mixing is calculated by summing over the full plasma region within the last closed field line, weighted by the particle density,

$$\left\langle \frac{\Delta P}{P} \right\rangle = \frac{\sum N(^3\text{He}) \Delta P/P}{\sum N(^3\text{He})}. \quad (9)$$

For ^3He , the mean effective polarization loss anticipated in DIII-D is $\langle \Delta P/P \rangle = 1.0\%$.

The strengths of the HFI in other single-electron species that can occur during dissociation and ionization are listed in table 1. The HFI strength is by far the largest in ^3He . Since the polarization correction from the latter is only 1%, HFIs in the others can be neglected in a DIII-D demonstration experiment (which is detailed in sections 5 and 6). Furthermore, since the polarization loss decreases with the square of the field, as in equation (8), such HFI effects are expected to be irrelevant for ITER-scale machines that are designed to operate with about three times higher fields.

4.2. Polarization loss during the particle confinement period

A variety of possible depolarization mechanisms has been investigated theoretically. A summary of past work is given in [10] and the papers cited therein; recently, the issues have been revisited by Gatto [60]. There are essentially two mechanisms of concern that survive scrutiny, interactions with the tokamak walls and resonant interactions with plasma waves. The impact of these in large-scale (e.g. ITER) machines versus research tokamaks can be very different.

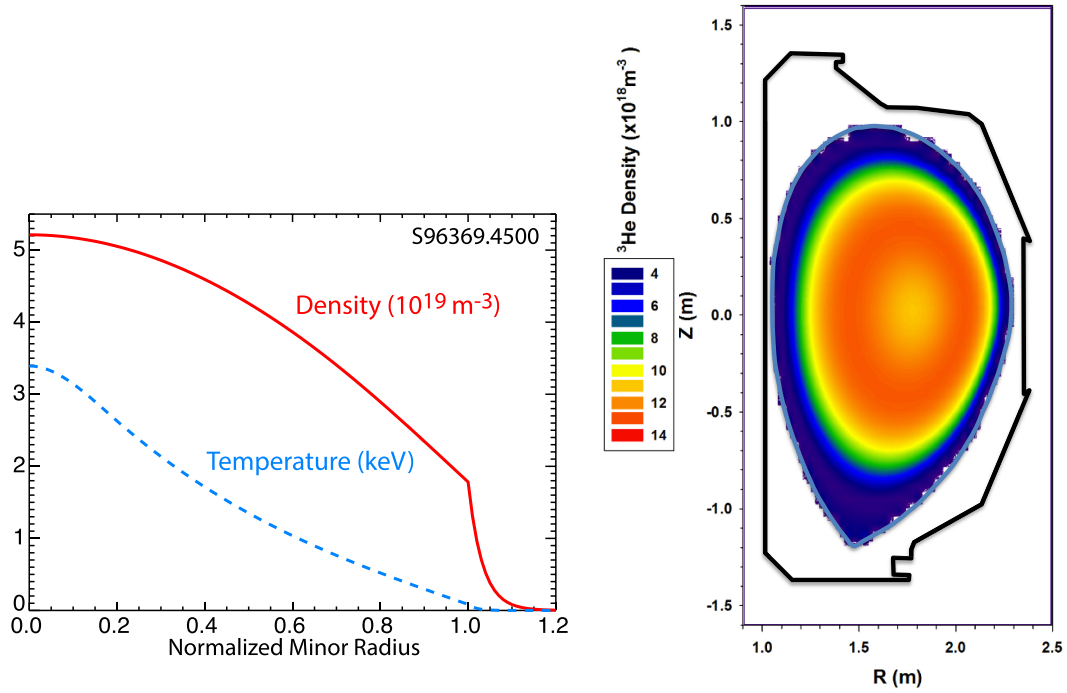


Figure 8. Left panel: electron temperature (dashed) and density (solid) versus normalized minor radius (ρ) for DIII-D Sh-96369, at $t = 4500$ ms, just prior to pellet injection at $t = 4550$ ms. Right panel: fuel density for Sh-96369 just after pellet injection at $t = 4575$ ms.

Table 1. Hyperfine interaction strengths in single electron species.

Species	A_{HFI} (GHz)	Reference
$^3\text{He}^+$	-8.665649867	[51, 55]
H	$+1.420405752$	[56]
D	$+0.327384353$	[57]
T	$+1.516701396$	[58]
HD^+	$A_p = +0.925456$ $A_d = +0.142273$	[59]

Following injection, a small fraction of the fuel mass undergoes fusion in the tokamak core while most of the ions leave the plasma without undergoing a nuclear interaction. The confinement time is much longer in the core than near the plasma edge, where it can be quite short. Upon reaching the walls, these ions pick up electrons and are neutralized. At the walls, there are several potential mechanisms that can, depending upon the structure and conditions of the wall material, lead to depolarization. However, the consequences of wall depolarization are moot in a high power ITER-scale reactor. ITER cannot be fueled by external gas jets (*gas puffing*) but must be fueled by pellets injected through the edge pedestal, because the Scrape-Off Layer is expected to be almost opaque to neutrals from the walls [61, 62]. In ITER, particles leaving the plasma will be swept to the diverter by convection so that the recycling of fuel from the walls, and hence the dilution of the polarization in the core, is expected to be essentially insignificant.

This is not necessarily the case in a lower-power research tokamak. Potential wall-depolarization mechanisms have been discussed extensively in [63], where low-Z, non-metallic

materials were expected to be optimal. Fortunately, the graphite walls of some research tokamaks, and DIII-D in particular, are well suited. Carbon has no conduction band, so that HFI with polarized material are eliminated. However, the material is porous and excessive dwell times at the wall could compound the chance of encountering paramagnetic impurities. But this can be mitigated by the deposition of a thin (100 nm) layer of boron on the walls, which has been shown to dramatically increase confinement times [64, 65]. The reduced dwell-time on a *Boronized* wall, coupled with modest energy confinement times in research machines such as DIII-D (~ 0.2 s), is expected to be effective in keeping wall depolarization at a minimal level for a research program of spin-polarized fusion studies.

The electron and ion charges generate electromagnetic waves when boosted into the frame of the plasma current. A particular class, the Alfvén eigenmode, arises from the periodic boundary conditions of the tokamak geometry. (See [66] for a recent overview.) When an ion's orbit is in phase with the eigenmode, their interaction can result in a larger displacement of the ion orbit, causing it to experience larger fluctuations in magnetic field. Several early papers [10, 67] speculated that excitation and amplification of these collective modes might be enhanced by the anisotropic decay angular distributions of figure 4, which could shorten depolarization times, particularly for tritium. Since they assumed many wall-plasma cycles, they concluded that triton depolarization could be significant. However, the main Alfvén eigenmodes are at a low frequency, compared to the cyclotron frequency, and $\Delta B/B$ during these orbits is on the order of 10^{-3} , which is not expected to lead to significant polarization loss. In any case, as discussed above, wall recycling in an ITER-scale tokamak is not

expected to be significant. Similarly, magnetohydrodynamic waves and microturbulence have frequencies too low to resonate with spin precession.

The plasma waves of concern are polarized collective emissions in the ion cyclotron range of frequencies, which are of the same order as the D and ^3He Larmor precessions. Waves of this type, known as Ion Cyclotron Emission (ICE), are often driven unstable by anisotropic fast-ion populations from neutral beams or fusion products [68]. When ICE is unstable, many cyclotron harmonics are usually observed. Under different operating conditions, ICE is emitted from different regions in the plasma. In DIII-D for example, ICE tends to be emitted from the center of L-mode plasmas but often is restricted to the outer edge of H-mode plasmas [69]. Since the spin precession frequencies vary with magnetic field, which drops as $1/R$ in a tokamak (as in figure 7), if the ICE propagates throughout the plasma, an ICE harmonic may resonate with a D or ^3He spin-precession frequency somewhere in the plasma. In practice, the mode properties of a plasma are highly variable, and a plasma in which specific modes are suppressed can be developed, albeit with effort. In particular, plasmas with and without ICE should be created with polarized fuels to assess the relevance of this depolarization mechanism.

5. Fueling an *in situ* test in a research-scale tokamak

In this section we describe a strategy for demonstrating fuel polarization survival in a research tokamak, using the DIII-D machine as a potential test bed. For the reasons discussed earlier, we choose $\text{D} + ^3\text{He} \rightarrow \alpha + \text{p}$ as the test reaction, using separate sources of polarized D and polarized ^3He injected into a high-temperature (>10 keV) hydrogen plasma. The resulting charged fusion products, particularly energetic protons, will have large gyro-radii and so will rapidly leave the plasma and can be detected at several wall locations. Suppressing some technical details, there are three key stages to such an experiment: the preparation of pellets of polarized D, preparing shells of polarized ^3He , each with sufficient spin lifetimes to make their loading into cryogenic injection guns practical, and the synchronized injection into a high ion-temperature plasma. Below we discuss each of these in turn.

5.1. Polarized D pellet fueling

We outline three methods of preparing polarized D for tokamak injection. The first two are straightforward adaptations of existing techniques that have been used to produce targets for NP experiments. Section 5.1.1 describes the use of Lithium-Deuteride as a carrier to deliver deuterium with 70% vector polarization. This would combine existing polarization, low-temperature and injection gun technologies, although their integration would necessitate a new engineering effort. Section 5.1.2 discusses the use of Hydrogen-Deuteride as the carrier to deliver deuterium with 40% vector polarization. This would require less of a construction project, mainly adapting existing equipment, but would involve many more stages and

would become more of a labor effort. (There are also *Stern–Gerlach* based molecular-beam methods of producing polarized D_2 that could in principle be utilized [70, 71], at least for a polarization survival test. However, since their fluxes are rather low, material would have to be collected over some time period without losing significant polarization, and a method would need to be developed to encapsulate the resulting polarized D_2 for injection. Because of such as yet unaddressed technical issues, they are not considered here.)

A third polarization method (section 5.1.3), with investment and development, promises to produce intense sources of D (or T) with essentially 100% polarization. In all methods, polarized material would be formed as cold pellets that could be injected with a cryogenic gun. In section 6, we conservatively model the proposed *Spin-Polarized-Fusion* (SPF) demonstration experiment assuming the conventional NP method of creating polarized D as discussed in 5.1.2, since this requires only the adaptation of equipment. Nonetheless, we include a condensed discussion of an *ultimate* method in section 5.1.3 and appendix D, to illustrate a path to a practical fueling scenario that could follow a successful confirmation of SPF.

5.1.1. Dynamically polarized Li D . Over the past decades, a variety of deuterated molecules have been used to create solid targets of polarized deuterium for NP experiments [15], the most commonly used being ammonia, ND_3 . These utilize a *dynamic nuclear polarization* (DNP) process, in which molecular electrons are first polarized in a magnetic field (\sim several tesla) at relatively low temperatures (~ 1 K) and microwaves are then used to drive a hyperfine transition that transfers their spins to the deuterons. However, the extraneous high Z atomic species that accompany the polarized deuterium in such molecules generally have high ionization energies and radiation losses that can act as sinks for power and can even potentially quench a plasma. For a SPF demonstration experiment, the most attractive of this class of material is Lithium-Deuteride, Li D . This material has reached the highest deuteron-vector polarizations reported, 70% [15]. Furthermore, not only does Lithium have relatively few electrons to alter the balance of the plasma, but it can in fact be a desirable addition, since Lithium injection is routinely used to improve wall conditions and mitigate *Edge Localized Modes* (ELMs) in tokamaks [72]. In terms of background fusion processes, only $^3\text{He} + ^6\text{Li}$ leads to protons with energies comparable to those from $\text{D} + ^3\text{He}$. These can be eliminated by using $^7\text{Li D}$ as the deuterium carrier, leaving ~ 15 MeV protons as a clean signature of $\text{D} + ^3\text{He}$ fusion. (Lithium is also polarized in the DNP process, but Radio-Frequency (RF) transitions could be used to erase the ^7Li polarization just prior to tokamak injection. Thus, while background processes can contribute to the low-energy alpha yield, the polarization dependence would come solely from $\text{D} + ^3\text{He}$.)

Lithium-deuteride is a solid at room temperature and can readily be formed into mm-scale pellets suitable for a SPF study. The DNP process requires the introduction of a small fraction ($\sim 2\%$) of paramagnetic centers. These are created

by radiation exposure at ~ 190 K, after which the material can be stored indefinitely at 77 K. With DNP, the polarization grows with time as $P_0(1 - e^{-t/T_1(D)})$, where $T_1(D)$ is the spin-relaxation time and P_0 is a limit determined by the polarizing conditions (field, temperature, microwave spin-transfer efficiency, etc). At 1 K and 5 tesla, deuteron vector polarizations saturate at about 50% in a few hours, and $T_1(D)$ is much longer than the typical duration of plasma shots at a research tokamak such as DIII-D (~ 20 s). Reaching the published maximum polarization of 70% would require DNP at 0.2–0.3 K and 6–8 tesla [73, 74], with longer buildup times of 1 -to- 2 d. Thus, one could imagine an experiment that is *tuned* and refined at $P_V(D) = 50\%$, followed by a limited number of $P_V(D) = 70\%$ shots requiring a longer spin buildup overhead. (Alternatively, multiple high-polarization ^7Li D pellets could be prepared simultaneously and stored for subsequent injection, although that would require another layer of equipment.)

The use of ^7Li D as the carrier for polarized deuterium would require a custom engineered polarizer, incorporating a DNP microwave circuit with RF coils that generate *Nuclear Magnetic Resonance* (NMR) signals for polarization monitoring and spin manipulations, coupled to a dedicated cryogenic injection gun, with a pellet handling system for multiple shots in one production cycle. The low operating temperatures of the polarizer would require either ^3He - ^4He dilution cooling to reach ~ 0.2 K, or a pumped ^3He system operating at ~ 0.3 K. (Neither of these are particularly challenging.) In the polarizer, the ^7Li D sample would need to be centered within a 6–8 tesla superconducting solenoid. While fringe fields from such a magnet might be of concern for plasma operations, since the bore of the solenoid could be small, this would require a relatively low inductance magnet that could be ramped down quickly (or even intentionally quenched) following the transfer of polarized pellets to the injection gun. The latter could operate at ~ 2 K without noticeable loss in polarization over the short period (tens of seconds) preceding injection.

The number of deuterons in such ^7Li D pellets is listed in table 2; 10^{20} is readily achievable.

5.1.2. Pellets of frozen-spin $H \cdot \vec{D}$. Solid HD is not dynamically polarized, but rather is brought to a *frozen-spin state* at very high fields (15 tesla) and low temperatures (0.010 K). HD samples that have completed a polarizing cycle can be transferred out of these extreme conditions and maintained at modest fields (~ 0.1 tesla) and temperatures (\sim few K), with deuterium spin-relaxation decay times on the order of months at 2 K [16]. HD is a gas at room temperature and must be contained in order to pass through the multi-step polarizing process. Polymer shells, originally developed for ICF, can provide an effective vessel.

We first consider diffusing about 400 bar of molecular HD into 2 -to- 3 mm diameter *Glow-Discharge-Polymer* (GDP) shells, manufactured by General Atomics (GA) [20]. The subsequent polarization of HD requires removing heat at low temperatures. The much larger HD targets that have been used

for NP experiments are cooled through contact with aluminum wires that thermally connect HD to a heat sink [16]. Alternatively, the cooling of SPF pellets can be achieved by adding ^4He gas, which at polarizing temperatures becomes a superfluid liquid. Such HD pellets can be cooled to a solid and transferred to a dilution refrigerator + superconducting magnet system where they can be polarized at ~ 10 mK and 15 tesla, using the NP techniques discussed in [16]. After the spins have become *frozen*, they can be cold transferred to another cryostat where RF excitations can be used to increase the deuteron polarization by transferring H spin to D [75]. A net deuteron vector-polarization of about 40% is expected. These pellets could then be shipped in a suitable cryostat to San Diego, loaded into a 2 K cryogenic pellet injector and fired into the DIII-D tokamak with a cold, supersonic helium gas jet [21]. Apart from the filling of a thin-walled GDP shell with high pressure HD (and ^4He), this stage just amounts to creating a small NP target with standard technology. The very long frozen-spin lifetime of such NP material (\sim months) allows the pellet polarization facilities and the tokamak to be separated by any distance, even thousands of km.

The characteristics of GDP shells are discussed in appendix C. When injecting these into a research tokamak it is necessary to keep the amount of shell material to a minimum, so that the large ionization energy of the carbon atoms of the shell wall does not become a sink for power and quench the plasma. Thin-walled shells can be filled by controlling the temperature-dependent permeation rate. They are typically evacuated at room temperature by simply pumping on their storage container, and then filled with the gas of interest—in this case, a mixture of about 90% HD and 10% ^4He , the latter insuring the required thermal conductivity at the low polarizing temperatures. The characteristic permeation time constant (τ) depends linearly on shell dimensions, and inversely on both temperature and a temperature-dependent permeation coefficient, $\tau = Dw/(6K_pRT)$. Here D is the diameter of the shell and w the wall thickness, R is the gas constant, T is the temperature, and $K_p = K_0 \cdot \exp(-\varepsilon_p/k_B T)$ is the permeation coefficient, with chemical activation energy ε_p (eV). (See appendix C for further details.)

Permeation rates of ^3He , ^4He , and HD into 2 mm diameter GDP shells, with wall thicknesses varying between 16 μm and 29 μm , have been measured at Jefferson Lab (JLab) and results are plotted in figure 9 over a range of temperatures, together with a fit to the expected temperature dependence. (Details are given in appendix C.) At elevated temperatures such as 150 C (423 K), gas quickly penetrated into the pellets ($\tau \sim 20$ s), but as the shell temperature is lowered the wall becomes completely sealed ($\tau \sim 300$ yr at 77 K).

In a typical filling scenario, one would increase the gas pressure on the outside of a GDP pellet in steps of 2/3 of the buckling pressure and wait 3–5 permeation time constants for the pressure across the pellet wall to equilibrate. By repeating this sequence, a thin-walled (~ 0.018 mm), 3 mm diameter pellet can be filled at ~ 425 K with 400 bar of HD (and 40 bar of ^4He) in about 12 h.

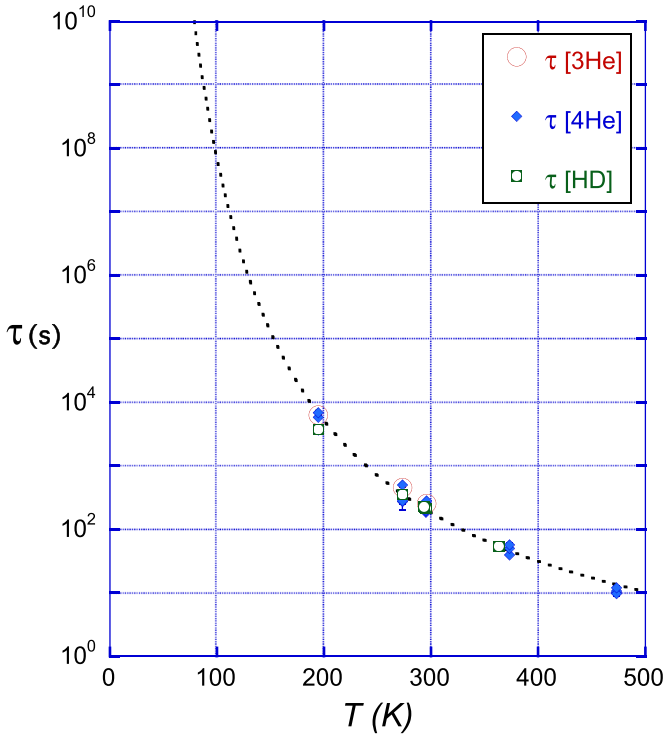


Figure 9. Permeation rates of ^3He , ^4He , and HD into 2 mm diameter GDP shells with wall thicknesses ranging from 16 μm to 29 μm . The dotted curve is a fit to the expected temperature dependence, as detailed in appendix C.

Cooling the permeation chamber to ~ 30 K reduces the pressure and increases τ to hundreds of years, completely sealing the pellet. At this point, the gas mixture outside of the pellets can be flushed and replaced with pure ^4He , keeping the pressure differential across the pellet wall well below the burst pressure of ~ 17 bar. Further cooling to the 16.6 K triple point of HD solidifies the HD on the inside wall of the pellet, and the ^4He pressure differential across the pellet wall becomes about 4 bar, which is still well below the expected buckling pressure of 6 bar. As the permeation chamber is cooled below 2.2 K the ^4He , both within and outside of the GDP shell, becomes superfluid and maintains efficient thermal contact with the walls of the chamber. The pellet then follows a routine NP target sequence to polarize the HD until it is ready for transfer and shipment to the tokamak facility [16].

Such pellets would contain $\sim 10^{20}$ polarized deuterons. As shown in table 2, the accompanying unpolarized higher-Z material (Carbon from the GDP shell containing the HD) is much less than in the LiD scenario of section 5.1.1, although a significant quantity of Hydrogen would be injected in this case.

5.1.3. High-flux polarized \bar{D} . There is a significant potential for a new type of polarized source using molecular-physics techniques to reach unprecedented fluxes. In brief, deuterated (or tritiated) molecules can be Infra-Red (IR) laser-excited with circularly polarized light to a rotational state with unresolved hyperfine structure; these states then beat, and

polarization is transferred between rotation and nuclear spin. This beating can be interrupted by rapidly applying a modest magnetic field, and freezing the polarization on the deuteron (or triton). Polarized deuterons (or tritons) can then be separated by dissociating the molecules with an Ultra-Violet (UV) or visible laser. Since this can now be accomplished on the μs time scale, and no beam separation is necessary (as the polarization mechanism occurs within each excited molecule), it avoids the flux limitation of conventional (Stern–Gerlach type) methods that have been limited to low intensities to avoid collisional depolarization that occurs on the ms time scale in magnetic separation. Utilizing a recent revolution in high-powered lasers, the potential intensity gain over conventional atomic beam sources is about a factor of a million. A scenario for producing large quantities of highly polarized DT is outlined in appendix D.

5.2. Polarized ^3He pellet fueling

Hybrid Spin-Exchange Optical Pumping (SEOP) can be used to polarize ^3He [18]. With this technique, a glass bulb containing pressurized ^3He , together with small amounts of Rubidium and Potassium ($\sim 10^{14} \text{ cm}^{-3}$) and Nitrogen ($\sim 0.7\%$), is heated to about 475 K (200 C) to vaporize the alkalis. The Rb vapor is polarized with 795 nm circularly polarized light from diode lasers, and collisions with the alkali atoms transfer polarization to the ^3He , usually in the sequence $\text{Rb} \rightarrow \text{K} \rightarrow ^3\text{He}$. After several hours the ^3He polarization has saturated (at about 65% in the polarizer used for the studies reported below [19], although higher levels have been reported by other groups [76]), after which the temperature of the polarizing cell is lowered. The vapor pressures of Rb and K drop rapidly with temperature, so that at 293 K (20 °C) their concentrations are less than 10^{10} cm^{-3} and essentially negligible. At this point, the ^3He can be extracted from the polarizing cell and used to fill a GDP pellet, with the same general procedures described previously in the filling of HD shells. The key difference here is that the ^3He must be laser polarized *first* to avoid vaporizing the GDP shell, the polarization must survive permeation of the GDP wall material and, after the temperature has been lowered to seal the wall, the polarization decay time within the pellet must be sufficient to allow for transfer to a pellet gun and injection into a tokamak. The GDP pellet fabrication process is known to leave free radicals within the material of the shell wall. This potentially exposes polarized ^3He to trapped paramagnetic impurities, which can contribute to depolarization. Once inside the pellet, experience with NP targets has shown that scattering from confining walls can be an important limitation to the ^3He polarization lifetime [77]. Such wall relaxation effects are material dependent, and need to be investigated because of the high surface/volume ratio inherent to the small ICF pellets.

5.2.1. Polarization losses during pellet permeation from MRI. The permeation and polarization survival characteristics of ^3He in GDP shells have been studied using 2 mm diameter GDP pellets supplied by GA [78]. A clinical



Figure 10. The typical placement of a 2 mm diameter GDP pellet (which appears amber in this photograph) above a Pyrex bead within a 3 mm Inside-Diameter (ID) tube for permeation imaging.

Magnetic Resonance Imaging (MRI) scanner with a nominal field strength of 1.5 tesla at the University of Virginia (UVa) [19] has been used to track the filling process by generating 3D polarization images of GDP shells during permeation. We outline the highlights of these studies here; extensive details are described in [79, 80]. Measurements were performed in borosilicate glass assemblies which ended in a tube with an inner diameter of 3 mm that contained a GDP pellet, as shown in figure 10. The glass tube was connected to a valved buffer volume between the gas inlet port and the entrance to the chamber containing a pellet. The latter was surrounded by a pair of saddle-shaped RF coils tuned to the ^3He NMR frequency. After evacuating the gas from all of the glass sections, and from the GDP shells in the process, the buffer volume was filled with room-temperature polarized ^3He gas while isolated from the pellet region, and then rolled into the scanner so that the pellet and the RF coils reached the isocenter of the MRI magnet system. Only then was the buffer valve opened, flooding the GDP pellet region with polarized gas. In this way the permeation process could be actively imaged.

Imaging results from a tube containing an 18-micron thick wall \times 1.8 mm diameter GDP pellet are shown in figure 11. The MRI was performed using a *chemical shift imaging* pulse sequence, which provides both spatial and spectral information. Frequency shifts induced by the presence of the Pyrex bead allow the spins inside and outside the GDP shell to be tracked separately. (Details of the MRI process are given in appendix E.) Figure 11 shows 2D images at a vertical slice containing the GDP pellet of figure 10. (The intrinsic resolution is $0.5 \text{ mm} \times 0.5 \text{ mm}$. The images have been interpolated to finer pixel size using standard MR image processing algorithms. The original pixelated images are reported in [79, 80].) The top row shows the total signal at each location versus time, obtained by summing the signal magnitude over the entire frequency spectrum originating from each voxel. The overlaid circle indicates the location of the pellet. This signal increases at the pellet location for about the first 8 min, corresponding to ~ 2 permeation time constants at room temperature, and then begins to fall.

The frequency-resolved polarization densities from spins inside and outside the GDP shell are plotted in the middle and bottom panels of figure 11, respectively. The sequence of images in the bottom panel reveal the decay (*longitudinal*

relaxation) of spins in the glass tube, with exponential time constant T_1 . The images in the middle panel clearly show the action of two time-dependent processes, permeation of spins into the pellet and their room-temperature relaxation. The former has been measured independently for the GDP pellet of figure 11, $\tau_{\text{perm}} = 3.78 \pm 0.07 \text{ min}$. (following appendix C). The latter is dominated by the T_1 relaxation of gas in the tube, $T_1^{\text{tube}} = 27 \pm 1 \text{ min}$ for the tube of figure 10, since at room temperature ^3He is continually exchanged across the pellet wall from an essentially infinite spin reservoir outside the pellet.

A comparison of the ^3He polarization density within the pellet, integrated over the frequency shifted *intra-pellet* peak, and the spin density outside the pellet gives the fractional loss in polarization during the permeation of the pellet wall, $22 \pm 1\%$ for the $18 \mu\text{m}$ -wall GDP pellet of figure 10. The loss in pellets with thicker walls increases roughly in proportion to the increased permeation time [79, 80], when filled at the same temperature. The pellet material is known to contain potentially depolarizing free radicals and the time that the ^3He spends within the GDP material is the crucial factor. However, since the permeation time is a strong function of temperature (e.g. figure C1 of appendix C), it should be possible to keep polarization losses in thicker walled pellets to a minimum by filling them at an elevated temperature.

5.2.2. Spin lifetime of encapsulated ^3He at 77 K. Once a pellet is filled with polarized ^3He , the temperature must be lowered to seal the GDP shell (as in figure 9). To be useful, the lifetime of the encapsulated spins must then be long enough to allow transfer of such polarized pellets to a gun for tokamak injection.

Further imaging measurements were carried out, using the same arrangement as described above. A $17 \mu\text{m}$ -wall \times 1.8 mm diameter GDP shell, positioned on top of a 3 mm solid glass bead (similar to figure 10), was positioned at the isocenter of the MRI scanner, after which the valve separating the ^3He buffer volume was opened to the pellet region of the tube. An initial 2D image is shown in the left panel of figure 12, taken $\sim 1 \text{ min}$ after the tube was flooded with polarized gas. The solid glass bead appears as the opaque sphere at the bottom. Above this is the GDP pellet in the early stage of permeation. After about two permeation time constants, the end of the tube containing the pellet was immersed in liquid N_2 . The gas within the tube provided a thermal coupling between the GDP shell and the tube walls, which quickly lowered the pellet temperature to 77 K, sealing the pellet wall. Then, $\sim 15 \text{ min}$ after the initial introduction of ^3He , the tube was evacuated, reducing the pressure outside the GDP shell to a few mb, which was sufficient to maintain thermal contact with the glass tube wall at 77 K, while contributing negligible extra-pellet signal to subsequent imaging. A 2D image taken $\sim 2 \text{ min}$ later (middle panel of figure 12) shows polarized ^3He confined to the pellet. Another image, with the same intensity scale, taken 6 h later is shown in the right panel, from which it is clear that very little polarization decay has occurred since the ^3He was sealed within the pellet.

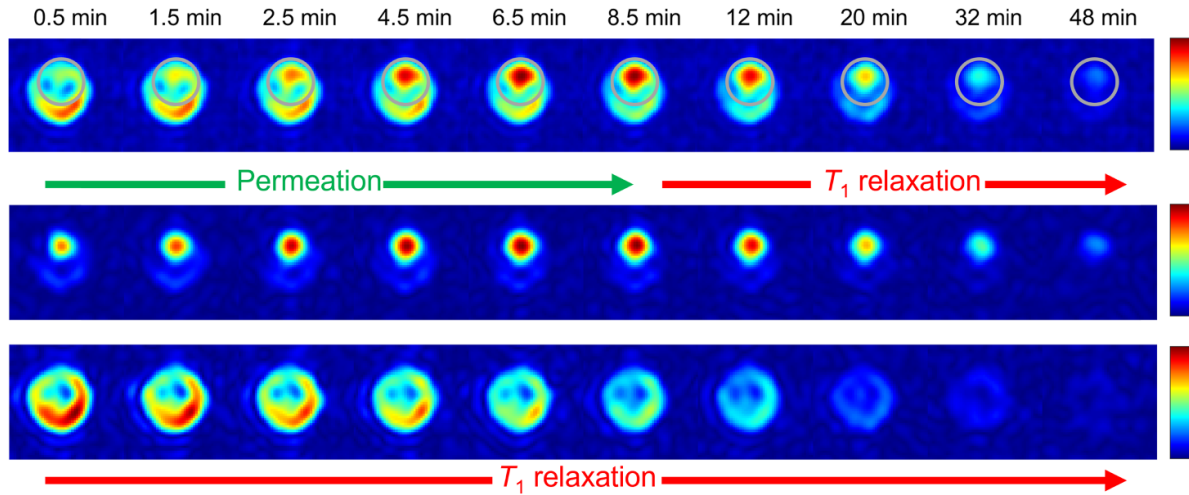


Figure 11. Imaging results obtained during the permeation of polarized ^3He into a GDP pellet with $18\ \mu\text{m}$ wall thickness and $1.8\ \text{mm}$ diameter. Top row: concatenated image series showing the total ^3He signal at the indicated times after the initial introduction of gas into the sampling tube of figure 10. A red color indicates higher polarization density. Circles indicate the position of the pellet. Frequency-resolved signals originating from ^3He spins located inside and outside the pellet are shown in the middle and bottom panels, respectively. (These are shown after interpolation with standard MR imaging algorithms; unprocessed images are pixelated, as in [79, 80].)

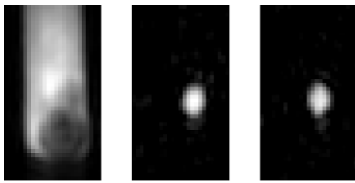


Figure 12. Left panel: a 2D MRI scan of a $17\ \mu\text{m}$ -wall $\times 1.8\ \text{mm}$ \odot GDP pellet on top of a $3\ \text{mm}$ \odot solid glass bead, within a glass tube similar to that of figure 10, is shown just after the tube was flooded with polarized gas. The white regions indicate the presence of polarized ^3He . After this image was obtained, the gas was allowed to permeate the GDP pellet for $\sim 10\ \text{min}$ before cooling to $77\ \text{K}$ by immersing the tube in liquid N_2 , which sealed the pellet wall. About $5\ \text{min}$. later, the gas outside the pellet was evacuated. Middle panel: a 2D MRI scan taken at $77\ \text{K}$, $\sim 15\ \text{min}$ after the initial introduction of polarized ^3He , and just after removing the ^3He gas outside the pellet. Right panel: a 2D MRI scan taken at $77\ \text{K}$, $6\ \text{h}$ after removing the gas outside the GDP pellet. The intensity scale of the right panel figure is the same as that in the middle panel.

The longitudinal relaxation of the spins within the GDP pellet at $77\ \text{K}$ was tracked with a simplified NMR measurement at regular intervals over a span of $10\ \text{h}$. (Imaging was not necessary since the pellet was the only source of ^3He polarization.) Each RF excitation flips a small fraction of spins, and so consumes hyperpolarized magnetization. Thus, each RF burst decremented the ^3He polarization, although by less than 0.5% . Even though each such loss is small, taken together they are not negligible compared with the longitudinal relaxation that occurred over the duration of the experiment. Nonetheless, correcting for them is straight-forward [79, 80].

Fitting such corrected data to an exponential decay gives a longitudinal relaxation time of the ^3He polarization in the GDP pellet as $T_1 \sim 3\ \text{d}$ at $77\ \text{K}$. (For comparison, the result without the RF-loss correction would have been $\sim 2\ \text{d}$ [79, 80].)

A $77\ \text{K}$ spin relaxation $T_1(^3\text{He})$ of $\sim 3\ \text{d}$ is extraordinarily long for a confining cell with such a high surface-to-volume ratio. This is likely associated with the extremely smooth surface of these shells that have been produced for ICF applications. Fortunately, such long $T_1(^3\text{He})$ times provide a manageable window for loading a cryogenic tokamak injection gun.

5.2.3. ^3He -fuel pellet preparation for a SPF demonstration experiment. The results in the previous sections demonstrate that polarized ^3He can be encapsulated in GDP shells. The MRI techniques discussed above provide a method of monitoring the expected polarization loss as hyperpolarized ^3He is permeated through the walls of GDP pellets. As discussed in appendix E, to actively monitor permeation in mm-scale pellets with sufficient spatial resolution, the geometry of these loss measurements must be restricted to small gas volumes, and these have relatively short room-temperature polarization relaxation times ($T_1 \sim 1/2\ \text{hr}$). In the measurements discussed in section 5.2.1, this resulted in the decay of about half of the available polarization before the GDP shell could reach its full pressure. GDP pellets intended for tokamak injection would be prepared in a substantially larger volume of about a liter, with an expected T_1 of $\sim 125\ \text{h}$ (as scaled with $[\text{surface}/\text{volume}]^{-1}$ and $[\text{pressure}]^{-1}$ from [81], although larger values have been reported [76]). In parallel, polarization loss during permeation would be monitored for a sampling of the GDP shells using an MRI system similar to that described above.

The fractional polarization loss is roughly proportional to the time the ^3He gas spends within pellet wall material, which depends both on the wall thickness and the permeation temperature. We illustrate the production of GDP shells with $18\ \mu\text{m}$ wall thickness for tokamak injection, using the model calculations of [79, 80].

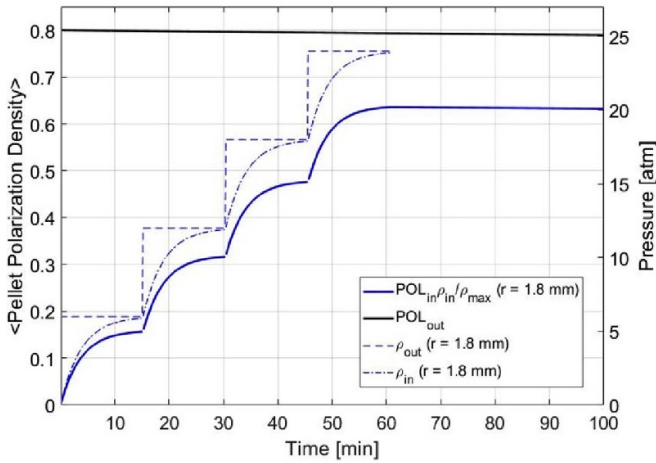


Figure 13. Expected ^3He polarization growth as shells are filled to 24 bar at 295 K in steps to avoid implosion, with the exterior and interior pressures (ρ) illustrated by the dashed and dashed-dot curves (as in the legend). The model of [79, 80] is used to account for polarization losses during permeation of GDP pellets with $1.8\ \mu\text{m}$ thick walls, and diameters of 1.8 mm. The mean polarization density is shown as the solid blue curve.

The polarizer used for the measurements discussed in the previous sections was limited by the requirements of its original medical imaging application. For a tokamak demonstration experiment an optimized SEOP ^3He polarizer can be constructed. ^3He polarizations up to 85% have been demonstrated, using frequency-narrowed diode laser pumping of volumes of about a liter [76]. For these calculations we assume a polarization performance of 80% at 25 bar, in a cell with T_1 of 125 h at room temperature. For $18\ \mu\text{m}$ wall \times 1.8 mm diameter shells (e.g. the GDP pellet of figure 11), the buckling pressure is 9.2 bar. Permeation could take place in a series of steps, where the outside-inside pressure difference is incremented by 2/3 of the buckling pressure at each step, i.e. 6 bar. This is illustrated as the blue dashed curve in figure 13. Maintaining the pressure for 4 permeation time constants ($=4 \times 3.8$ min at 295 K for this shell) fills a pellet to 98.2% of the exterior pressure at each step (the blue dashed-dot curve), so that the interior pressure reaches 24 bar in about an hour at 295 K. The expected polarization growth profile for such a pellet, including the polarization loss during permeation, is shown as the solid blue curve in figure 13, and reaches about 65%. With the short permeation time, spins are constantly being exchanged across the pellet wall. Since the spin reservoir is huge compared to the volume of the pellet, the net T_1 of gas inside the pellet is essentially the same as that of the reservoir. A filled pellet can be cooled to 77 K with liquid nitrogen, at which point the pellet wall is sealed, the internal T_1 becomes ~ 3 d, and the internal pressure drops to 6.2 bar. Since this is substantially below the burst pressure of 27.6 bar, the exterior pressure can safely be lowered to the few mbar needed to maintain thermal contact with the 77 K container walls. At this point the pellet would be ready for transfer to a 77 K gun in preparation for tokamak injection.

The 1.8 mm Outside-Diameter (OD) GDP shells modeled in figure 13 contain $\sim 0.2 \times 10^{19}$ atoms of polarized ^3He . Larger shells with 3 mm OD and the same wall thickness could be filled in a similar manner to $\sim 1 \times 10^{19}$. This is about an order of magnitude lower than the number of polarized deuterons that could be injected (table 2), but this could partly be compensated by simultaneously firing multiple ^3He pellets. The latter is not so great a complication since the ^3He pellet injector only needs to operate at 77 K. In any case, the reaction rate is proportional to the product $N(\text{D}) \times N(^3\text{He})$, and so it is not essential that the two densities be identical.

Polarization loss during permeation limits the ultimate ^3He spin that can be encapsulated. However, as already mentioned, the GDP pellet production process leaves free radicals within the shell material. Those used in the measurements discussed above were stored in air prior to shipment to JLab, and in the presence of ambient light that catalyzes reactions with oxygen. Recent work has revealed the formation of O–H hydroxyl bond structures on the surface under these conditions [82]. The paramagnetic character of these O–H bonds is a likely source of depolarization. GDP pellets made specifically for ^3He encapsulation could reduce this loss simply with an improved storage environment prior to usage.

5.3. Injection of polarized pellets

An SPF demonstration measurement must be initiated by the injection of polarized D pellets, either as GDP shells containing solid HD or as solid ^7LiD pellets, followed quickly (within tens of ms) by polarized ^3He in GDP shells. Deuterium pellets can be injected at $\sim 2\text{--}4$ K, while ^3He would be injected at ~ 77 K. For a practical realization of such an experiment, it is likely that a dedicated injection gun would be constructed to operate at 2–4 K. Since reaching such temperatures requires a 70 K–90 K radiation shield, cooled either with liquid N_2 , boil-off liquid helium or by an intermediate cooling stage from a closed-circuit cryo-cooler, a single injection gun could be engineered to accommodate the injection of both polarized species. The gun would need to incorporate an internal magnetic field to maintain pellet polarizations, and a field of about 0.1 tesla would be sufficient. At 2 K and 0.1 tesla, the measured $T_1(\text{D})$ polarization decay time is about 2 months for frozen-spin HD [16]. For Li D, $T_1(\text{D})$ is proportional to $e^2\mu_e B/kT$, where μ_e is the magnetic moment of the paramagnetic electrons used in the DNP process. Scaling down existing higher field data [74], a $T_1(\text{D})$ of about 6 min is expected at 2 K and 0.1 tesla. For polarized ^3He at 77 K, $T_1(^3\text{He})$ is ~ 3 d, as reflected in figure 12. Although the latter result was measured at 1.5 tesla, the field dependence of $T_1(^3\text{He})$ is very weak and 0.1 tesla is in fact much larger than is typically used as a holding field in NP experiments [83]. While Li D has the most restrictions of these polarized species, its T_1 is still much longer than the time needed to transfer a pellet from an adjacent polarizer to an injection gun (~ 1 s), ramp down the polarizing magnet (~ 10 s), ramp up the DIII-D torus field (~ 7 s), and fire the cryogun (~ 1 ms).

In existing solid (unpolarized) D₂ pellet guns, samples are propelled from the 4 K barrel of a cryo-gun to the tokamak by room temperature helium gas [21]. Downstream of the ~ 0.5 m long gun barrel, room temperature guide tubes, with staggered differential pumping to remove the propellant gas, provide a vacuum envelop for the flight trajectory to the tokamak. A straight guide tube with a telescoping inner diameter avoids contacting the pellet during its \sim ms flight.

The guide tube following a new 2 K gun could remain at room temperature since it has no direct contact with the pellet and the radiation from the walls during the \sim ms transit time is very small. However, to minimize polarization loss, cold helium gas should be used to propel polarized pellets, and a triggered flash evaporation of liquid helium could be a possible source of cold pressurized propellant. The injection of polarized ³He pellets from a barrel cooled by the 70 K–90 K stage could follow a similar parallel path, with multiple tubes to guide several of the lower density ³He shells merging into the same guide tube.

The D and ³He polarizations must be maintained by a magnetic field throughout their flight path to the outer edge of the Tokamak. For deuterium, typically a few hundred gauss is sufficient; for ³He, even 25 gauss will preserve the in-flight polarization. Such fields can be generated by a solenoid winding wrapped around the guide tube, with a tapered wire density that decreases as the tube enters the fringe field of the tokamak. While injection velocities are typically ~ 500 to 1000 m s^{−1}, this and/or some tumbling motion down the guide tube are significantly slower than the Larmor frequencies of either D or ³He. As a result, the D and ³He spin vectors will adiabatically follow the net local field as the tokamak fringe field rises and the guide tube field falls. (See [16] for an example of spins transferred through different field orientations without loss of polarization.) Once inside the hydrogen plasma, the spins will align along the local magnetic field.

The anti-parallel spin configuration can be prepared within the cryo-gun, using an RF transition (an *Adiabatic Fast Passage*, or AFP) to flip the sub-state population so that the spin of the ³He (or the D, but not both) is aligned against the local magnetic field [75].

Pellet injection from various points in the DIII-D tokamak has been studied, and vertical injection (designated $V + 1$ in [21].) has several advantages for SPF. The pellet velocities are the highest, consistent with essentially no wall collisions along the straight guide tube, giving the pellet a high probability of entering the tokamak intact. (Experience with the injection of pellets on DIII-D has shown that shells with gas payloads have proved fairly robust, with few breaking prematurely during the flight down the guide tube, compared with shells containing loose solid material, which presumably reacts to the impulse of acceleration [84]. Nonetheless, in the case of HD pellets, the polarized material would be frozen onto the inside surface of the GDP shells, and so is not expected to be susceptible to this problem.) The $V + 1$ trajectory is on the High Field Side (HFS) of the plasma distribution and has a high fueling efficiency, compared with Low Field Side (LFS) injection in which more than half of the pellet mass is ejected [21].

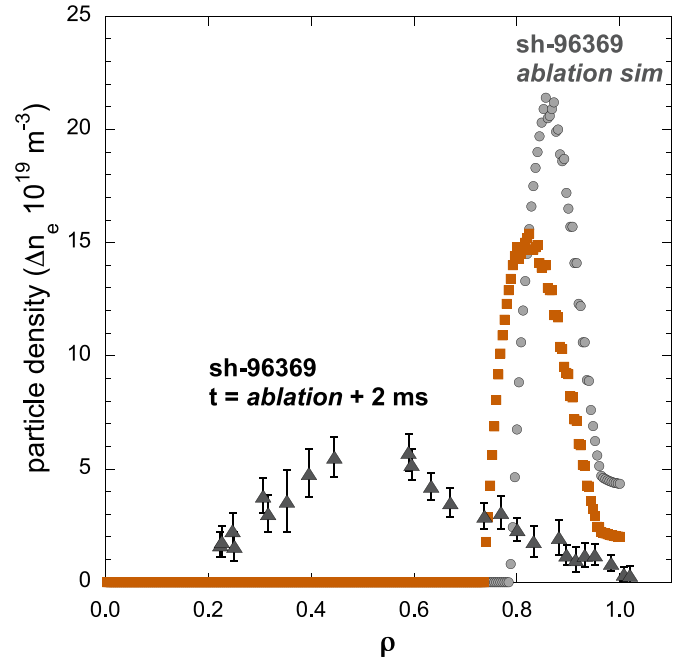


Figure 14. The calculated ablation of a 2.7 mm diameter solid D₂ pellet injected into DIII-D sh-96369, with T_e peaking at 3.4 keV (as in figure 8) is shown as grey circles. The change in n_e two ms after ablation, which reflects the incremental deuterium density from the pellet, is plotted as the black triangles. The calculated ablation of a 3 mm diameter D₂ pellet injected at 1000 m s^{−1} into a Q H-mode plasma, with T_e peaking at 4.0 keV [87], is plotted in orange.

Upon entering the plasma, the pellet ablation rate is determined by the temperature of the plasma electrons, $(k_B)T_e$. For the DIII-D shot shown in figure 8, sh-96369, T_e peaks at 3.4 keV immediately prior to injection of a 2.7 mm diameter solid D₂ pellet through the vertical $V + 1$ port. The calculated ablation profile of this pellet is shown in figure 14 as the grey circles [85], as a function of the normalized minor radius (ρ). Initially, the pellet material does not penetrate far into the plasma. However, the deduced deuterium density 2 ms later is plotted as the solid triangles [21]. (This is measured as the change in the number of electrons before and immediately after pellet injection, deduced from a Thompson scattering diagnostic.) This illustrates the effect of a fast transport mechanism that rapidly (< 1 ms) sweeps the pellet matter deep into the plasma, and is particularly effective for HFS vertical injection [86]. Similar data for LFS injection show much less penetration [21]. On a longer time-scale, 50–100 ms, diffusion driven by density gradients will transport the injected material inward, even from LFS injection. But to maintain the most sensitivity to possible depolarization time scales, injection through the vertical $V + 1$ port is preferred to leverage the fast transport process. Thus, vertical injection through the $V + 1$ port (a) achieves the highest velocities by eliminating contact with the guide tube, (b) enters the plasma on the HFS with high efficiency (little mass ejection), and (c) is accompanied by a rapid transport into the plasma of the injected material.

Table 2. Achievable number densities, particles per fuel pellet in units of 10^{19} , are listed with their degree of ^3He or D polarizations for different pellet diameters. For deuterons, both vector and tensor polarizations are given. The quantities of extraneous accompanying material from the deuteron carrier and/or the shell material are also tabulated. The different polarization processes are discussed in section 5.1.1 for ^7Li D, in section 5.1.2 for H D, and in section 5.2 for ^3He .

Carrier	Pellet ⊙ (mm)	Shell	${}^3\vec{He}$		\vec{D}			Extraneous material			
			# ${}^3\vec{He}$ ($\times 10^{19}$)	$P({}^3He)$ (%)	# \vec{D} ($\times 10^{19}$)	$P_v(D)$ (%)	$P_T(D)$ (%)	# 4He ($\times 10^{19}$)	# H ($\times 10^{19}$)	# C ($\times 10^{19}$)	# 7Li ($\times 10^{19}$)
${}^7Li\ D$	1.0	—			3.2	70	41				3.2
${}^7Li\ D$	1.5	—			10.7	70	41				10.7
HD	1.8	GDP			2.1	40	12	0.2	3.1	0.9	
HD	3.0	GDP			9.8	40	12	1.0	12.6	2.8	
3He	1.8	GDP	0.18	65					1.0	0.9	
3He	3.0	GDP	0.85	65					2.8	2.4	

5.4. Extraneous material accompanying polarized pellets

Injected ^3He shells (section 5.2), and either option for polarized Deuterium, ^7Li D (section 5.1.1) or HD (section 5.1.2), would introduce extra material into the plasma, the quantities are summarized in the last four columns of table 2. The Li D pellets introduce the most higher-Z material, although at $Z = 3$ Lithium has little detrimental impact. Furthermore, since separate Lithium injection is routinely used to suppress ELMs [72], both species in a Li D pellet injection could have a beneficial role. The HD shells have the lowest amounts of higher-Z material, coming from their GDP casing, although these pellets introduce appreciable quantities of Hydrogen that could lower the average ion temperature.

6. Plasma requirements and detection strategies

The previous section presents cost-effective ways to utilize existing NP methods to generate polarized material in a form suitable for injection into an unpolarized plasma. In this section we consider the requirements of a hypothetical DIII-D experiment, in which polarized D and polarized ^3He are injected. Historically, the vast majority of discharges on DIII-D have utilized a deuterium plasma. This presents the first hurdle that must be overcome to enable a SPF measurement. Since all thermal deuterons are indistinguishable, the net polarization of injected deuterium would be immediately diluted by the mass fraction upon entering a D plasma. While some DIII-D studies have been devoted to H plasmas, they have tended to be more problematic and more development work is needed, particularly to establish the high T_{ion} modes necessary to generate adequate fusion yields. A ^4He plasma is another possible option that would not contaminate $\text{D} + ^3\text{He}$ fusion product yields, although so far experience with helium plasmas is minimal.

6.1. Strategies for detecting polarization in a plasma

Polarization alters both the fusion yields, equation (5), as well as the angular distribution of the fusion products, equation (4). Each of these changes provides a potential *signal* for SPF. In subsequent sections we investigate an approach to detecting

the presence of polarization in a plasma by comparing the fusion rates between successive plasma shots in which D and ^3He are injected with their spins oriented alternatively parallel and anti-parallel. Assuming the anticipated polarizations of D and ^3He summarized in table 2, $P_V(\text{D}) = 70\%$ with a ^7Li D carrier (section 5.1.1), or $P_V(\text{D}) = 40\%$ with an HD carrier (section 5.1.2), and $P(^3\text{He}) = 65\%$ (section 5.2), the simple expectation for the dependence of the fusion rate on polarization, ignoring variations in the efficiency for charged fusion products to reach the walls, would be (from equation (5)),

$$\frac{\langle \sigma^{\text{par}} \nu \rangle}{\langle \sigma^{\text{anti}} \nu \rangle} = 1.59, \text{ from } ^7\text{LiD} + ^3\text{He} \text{ pellets,}$$

$$\frac{\langle \sigma^{\text{par}} \nu \rangle}{\langle \sigma^{\text{anti}} \nu \rangle} = 1.30, \text{ from HD} + ^3\text{He} \text{ pellets.} \quad (10)$$

Such a comparison requires a sequence of plasma shots that are *equivalent*, to within some modest systematic uncertainty.

However, at DIII-D, each shot has tended to be an experiment of its own, and plasma parameters are rarely deliberately held fixed. A mining of past DIII-D data has yielded very few successive shots in which such comparisons can be made. This leaves the systematic uncertainty between nominally *identical* plasma shots as rather poorly determined at present. Accordingly, in the subsequent sections we model the number of shots that would be required with this measurement strategy, using different assumptions for systematic variations.

An alternate detection strategy envisioned in a companion paper [26], exploits the polarization dependence in the angular distribution of emitted fragments (figure 4). Simulations in [26] show that the pitch at the tokamak wall, taken as the arccos of the parallel component of the ion velocity v_{\parallel}/v , is strongly correlated with the polar reaction angle at birth. Since the dependence of the cross section on this angle is strongly polarization dependent, as in equation (4) and figure 4, the shape of the v_{\parallel}/v velocity distribution at a fixed location on the tokamak wall varies with polarization. The ratio of the flux at detectors that are poloidally separated (normal to the toroidal field) also depends upon the polarization. Comparisons between shots with polarized and unpolarized fuel then reveal relative changes in the shape of fusion-product angular distributions, even if the plasma characteristics are

appreciably different, as opposed to absolute rate measurements from similar plasma shots which are required for the ratios of equation (10). There are several options for monitoring fusion products at the plasma-facing wall. Both Fast Ion Loss Detectors [88], and Silicon surface barrier detectors have been successfully used at DIII-D [89]. Of course, in an actual experiment, all available information would be used: changes in total reaction rate from similar discharges, comparisons with rates calculated from T_{ion} , n_{He} and n_{D} , and relative signals that depend upon the differential cross section.

For completeness, we mention another possible polarization detection strategy, using an RF antenna within the tokamak to carry out NMR measurements on polarized ions present in the plasma [90]. In such a measurement, an RF pulse would tip a fraction of spins out of their preferred alignment with the local magnetic field, and the antenna would detect their resulting precession. For a fully polarized ^3He plasma in Alcator C-Mod, assuming that can be created somehow, estimates project that NMR signals of order $10\ \mu\text{V}$ could be generated [90]. However potential backgrounds are significant; the largest from ICE is estimated at twice the NMR signal. In practice, with NMR measurements, signal/noise is the deciding factor. NP experience has shown that backgrounds usually increase significantly when moving polarized material from an isolated lab to the environment of an accelerator, or presumably a tokamak, where large arrays of complex equipment are in use. Such *non-physics* noise is generally time-varying, essentially impossible to predict, and is often the real limiting factor. We view this approach as very challenging.

6.2. Simulation of polarization-dependent fusion yields

In this section we model how changes in fusion yields due to polarization would be reflected at the walls of the DIII-D tokamak. (The effects of changes in the angular distribution are treated separately in [26].) Our goal here is to demonstrate that the basic enhancements of equation (10) are reflected at the plasma-facing wall, despite the highly variable orbits of the charged fusion products through the tokamak. By tracking fusion products emitted over the full range of birth angles through the tokamak fields, we determine the efficiency for protons and alphas to reach different points on the wall from different locations within the plasma. (In NP language, this determines the *acceptance* of DIII-D.) This provides wall-location dependent corrections to equation (10). Here we have conservatively modeled the option of section 5 with the lower deuteron polarization, the scenario expected from the injection of HD and ^3He .

6.2.1. Plasma parameters for modeling and simulation. We consider a notional DIII-D experiment heated by hydrogen neutral beam injection into a majority high ion-temperature hydrogen plasma with minority ^3He and D populations from polarized pellets. These plasma characteristics have not yet been achieved in DIII-D. (Some of the associated challenges are discussed further in the companion paper [26].) Modeling begins with plasma characteristics from sh-96369, a past

DIII-D shot with a solid D_2 pellet injection through the HFS $V + 1$ vertical port at $t = 4550\ \text{ms}$ [21], into a deuterium plasma. (The electron temperature and density for this injection are shown in figure 8.) For a high- T_{ion} Q H-mode plasma, T_e can be expected to peak at about 4 keV [87]. With this T_e , the calculated ablation profile of a 3 mm diameter pellet injected through the $V + 1$ port at $1\ \text{km s}^{-1}$ is shown in orange in figure 14. Comparing ablation and deposition profiles in sh-96369 (grey and black triangles in figure 14), the $V + 1$ injection efficiency is expected to be high in our modeled case and the fast transport mechanism is expected to quickly sweep material deep into the plasma (section 5.3).

The modeling scales parameters as necessary to predict the outcome of the hypothetical experiment. This involves a calculation of the instantaneous fusion rate and then an orbit-following calculation of the charged fusion products. To model the fusion rate, the data from the injection shown in figure 14 has been used. This is simulated with the power balance code ONETWO [91, 92], in which the injected pellet is treated as providing a ^3He impurity, scaling ion energies and cross sections to represent $\text{D} + ^3\text{He}$ reactions. The effective number of each species present in this simulated condition is about 6×10^{20} , the particle number injected into shot 96369. (This injection was in the form of a solid pellet without encapsulation, so none of the extraneous materials listed in table 2 are reflected in the simulation.) The fusion product orbits are then evaluated using a magnetic equilibrium that is calculated for the reference plasma by the EFIT code [52], which processes various plasma diagnostic measurements to determine the resulting flux surfaces and electric field profiles. (Here, the orbit trajectories are calculated without electric field profiles and collisional scattering, both of which generate only small corrections for the high energy $\text{D} + ^3\text{He}$ fusion products.) The resulting charged fusion product flux along the plasma-facing wall can then be compared between the parallel alignment and the anti-parallel orientations of initial D and ^3He spins.

Figure 15 shows the constructed ion temperature profile used to produce a large absolute fusion rate. In DIII-D, peak central ion temperatures of 15 keV have been achieved in a Quiescent H-mode deuterium plasma following deuterium pellet injection [87], and ion temperatures above 20 keV have been achieved in a deuterium plasma with internal transport barriers [93]. Optimistically, a peak ion temperature of 15 keV is modeled. Fusion rates have been scaled by the ratio of $\text{D} + ^3\text{He}$ -to- $\text{D} + \text{D}$ cross sections, and the resulting $\text{D} + ^3\text{He}$ fusion rate is shown as the red dashed curve in figure 15, where the horizontal axis, ρ , is the effective radial coordinate—the normalized value of the square root of the toroidal magnetic flux. The fusion rate is strongly peaked in the core, as expected given the sensitive dependence of the fusion cross section on ion temperature. This rate reflects the number of particles involved in shot 96369. From table 2, a single 3 mm diameter HD pellet and four 3 mm diameter ^3He pellets would yield flux densities that are a hundred times smaller.

6.2.2. Tracking fusion products in DIII-D. The fusion rate density of figure 15 is converted to a discretized function

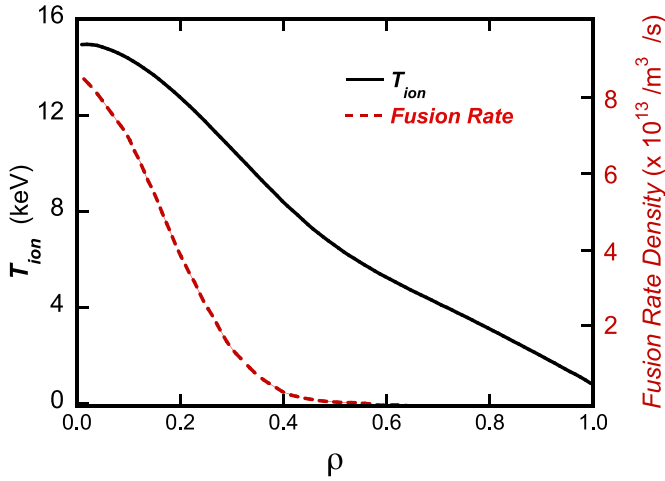


Figure 15. Ion temperature profile, with scale on the left, for the modeled case featuring the largest absolute fusion rate. This profile has been modified based on original data from shot 96369, scaling the peak ion temperature from 5 keV up to 15 keV. The resulting fusion rate is plotted as the dashed red line, with scale on the right. (One 3 mm diameter HD pellet and four 3 mm diameter ^3He pellets would yield flux densities that are a hundred times smaller.) The horizontal axis, ρ , represents the normalized value of the square root of the toroidal magnetic flux.

of major radius and vertical position and used to source the appropriate number of $\alpha + p$ fusion products. This provides the number of particles originating at each specific location; that number is then divided amongst the possible birth pitch and gyrophase angles, weighting their relative number by the polarized angular distributions of equation (4). The orbits of the α and p fusion products are then tracked through the DIII-D magnetic field until they strike the plasma-facing wall. Details of the orbit modeling are provided in appendix F.

The left panel of figure 16 shows the geometry of the tokamak as a cross-section of major radius and elevation. The right-panel plots two 14.7 MeV proton orbits. One proton originates at the magnetic axis and the other at $\rho = 0.4$ which, as is evident in figure 15, is about the approximate radial extent of significant fusion activity. Both protons have the same birth gyrophase for this example, and they reach the vessel wall at quite different poloidal positions.

The calculation of the wall strike positions for the full distribution of charged fusion products, integrated over pitch and gyrophase angles at birth, provides the poloidal profile of arriving particle flux. This is shown in figure 17 for protons (top panel) and alphas (bottom panel), for parallel and anti-parallel D and ^3He spins as the blue and red histograms, respectively. This simulation has assumed 40% deuteron vector polarization, with an accompanying 12% tensor polarization (from HD filled shells, as in section 5.1.2), and 65% ^3He polarization. As expected from equation (10), there is more yield when the initial D and ^3He spins are parallel (blue histograms). The patterns have a relative maximum above the 0° mid-plane (at positive poloidal angles), reflecting the characteristic *acceptance* of DIII-D when its magnets are energized so that the total magnetic field rotates counter-clockwise when viewed from above. (The pattern is reflection-symmetric with

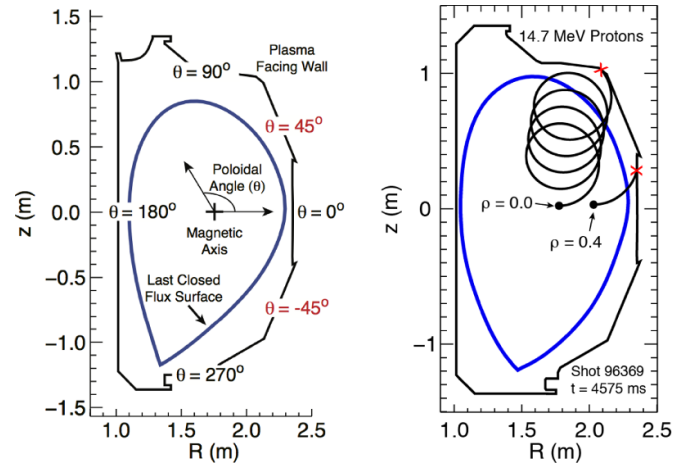


Figure 16. (Left) Tokamak geometry for the orbit modeling of $\text{D} + ^3\text{He}$ charged fusion products. Poloidal angles are defined relative to the midplane. (Right) Examples of toroidal orbits of 14.7 MeV protons, projected onto a 2D slice through the torus field, and striking different parts of the DIII-D wall.

field, so that the relative maximum would appear below the mid-plane if the energizing currents were reversed. The latter is assumed in the simulations of [26].)

The ratios of expected yields from DIII-D shots with anti-parallel and parallel D and ^3He initial spin alignments are shown in figure 18 for protons (top) and alphas (bottom) at different locations along the plasma-facing wall of the DIII-D vacuum vessel. The strong signal of equation (10) is maintained over a large range of wall locations. Although the departure of the ratio from unity extends well below the 0° mid-plane, the yields there are significantly smaller (figure 17). Thus, the existing DIII-D access ports at poloidal positions of 0° , 56° , 77° and 100° would be nearly optimum locations for particle detectors. If 70% vector-polarized deuterons were used (from ^7Li D pellets, as in section 5.2.1), these ratio profiles would be amplified significantly.

6.2.3. The consequence of shot-to-shot variations. The DIII-D tokamak is a research-scale reactor with room temperature coils. Each *shot* is initiated with a 3 s ramp up to 2.1 tesla, followed by a 10 s flat-field period in which ~ 80 keV neutral beams heat the plasma and measurements are carried out, and then a 7 s ramp down. There are then 15 min between shots to allow the coils to cool. To capitalize on the expected strong signals evident in figure 18 requires a comparison between multiple shots with very similar plasma characteristics.

The parameters that determine the thermonuclear reaction rate are the ion temperature T_{ion} , the ^3He density n_{He} , and the deuterium density n_{D} , integrated over the plasma volume. At DIII-D, Charge Exchange Recombination (CER) of carbon is used to monitor T_{ion} [94], while CER of helium can measure the helium profile n_{He} [95], and the main ion CER diagnostic can monitor the deuterium profile n_{D} [96]. One could imagine using profile measurements of these quantities to calculate the expected fusion rate, then normalizing fusion-product signals by calculated rates, although uncertainties in T_{ion} ,

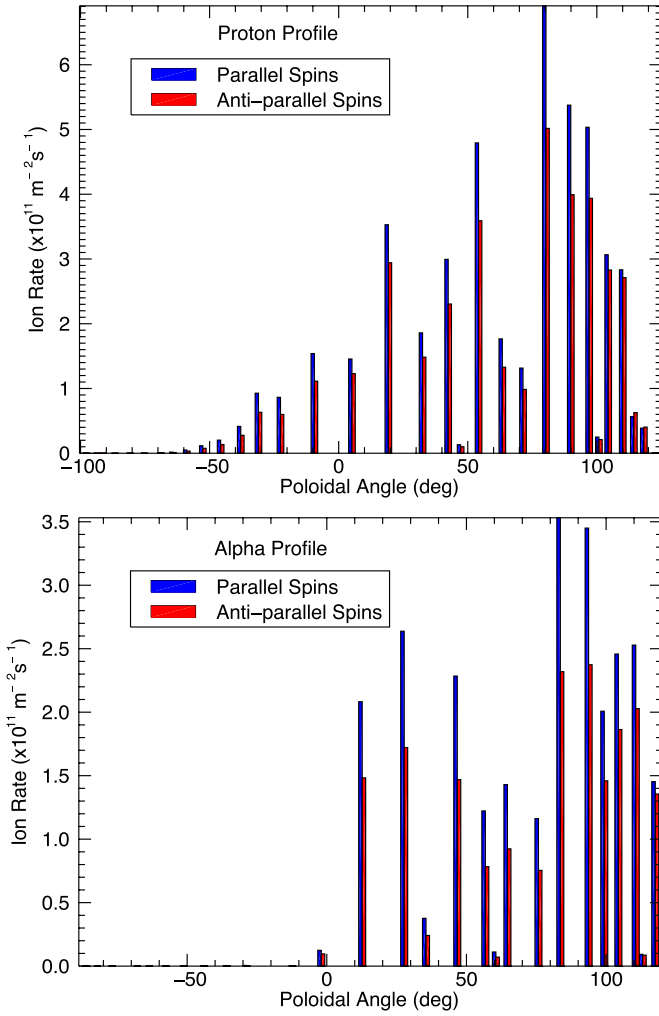


Figure 17. Yield of protons (top) and alphas (bottom) at the plasma-facing wall, integrated over birth pitch and gyro-phase angles, as a function of poloidal angle at the DIII-D vacuum wall, for initially parallel (blue) and anti-parallel (red) D and ^3He spin orientations. Wall strikes are binned in segments of 0.01 m^2 in area. (See appendix F for further details).

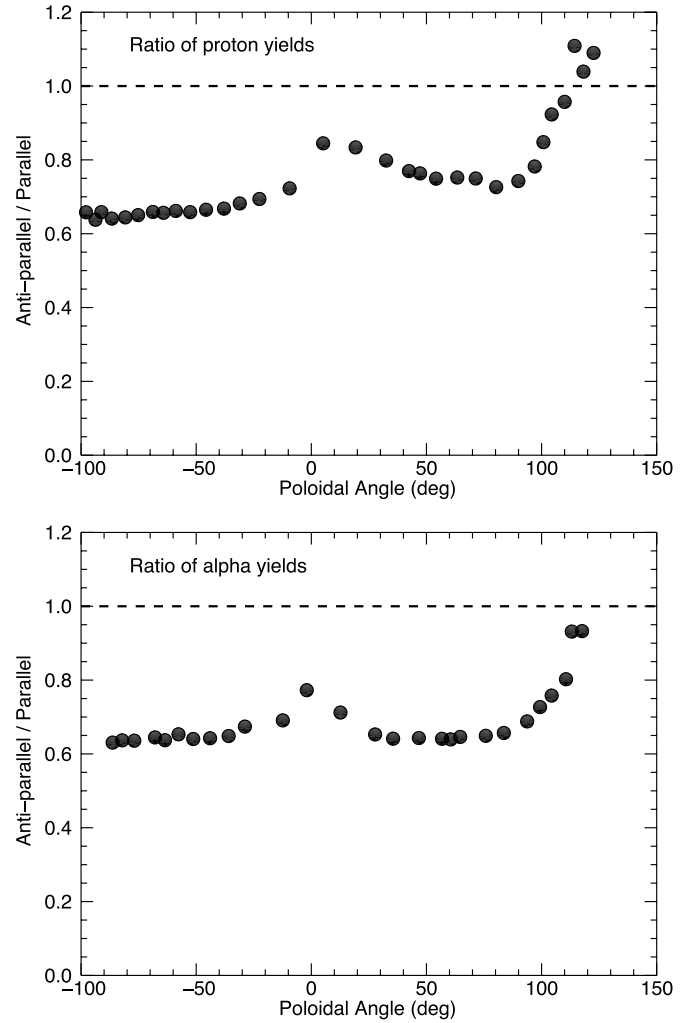


Figure 18. The predicted ratio of the high energy proton (top) and alpha (bottom) yields from successive plasma shots with D and ^3He spins anti-parallel and parallel, for different locations along the plasma-facing wall of the DIII-D vacuum vessel, shown in terms of their poloidal angle.

n_{He} and n_{D} could compromise the accuracy of the polarization measurement. In this section, we consider the alternative approach of selecting discharges that are *reproducible* within some selected systematic variation. As an example, two successive plasma shots are shown in figure 2 of [25], where ion current, electron temperature, the RMS amplitude of magnetic fluctuations, and electron density between the two shots are compared, and are clearly highly correlated. While H-plasmas heated with neutral H-beams will have to be optimized for SPF, it is clear that the DIII-D diagnostics are available to characterize each plasma shot. In this approach, optimizing a SPF experiment would be preceded by a systematic study to correlate plasma diagnostics with the thermonuclear fusion rates in proton and alpha detectors following the injection of unpolarized D pellets ($^7\text{Li D}$ or H D) and unpolarized ^3He pellets. In this way, shots with comparable plasma conditions can be selected when comparing fusion yields from different fuel polarizations.

The number of shots required to verify the predictions of figure 18 depends on the plasma variations one is willing to accept. A Monte Carlo simulation shows the effect of accepting larger shot variations for analysis. For a conservative estimate, the lower deuteron vector polarization of section 5.1.1 (40%) has been assumed here. The results are summarized in figure 19. With a pool of shots that have 8% systematic shot-to-shot variations in their fusion yields, a 5σ determination (the conventional criteria for ‘discovery’) is obtained with merely four plasma shots in each spin orientation. Of course, it is not yet clear how many hydrogen plasma shots will be required before accumulating four in each spin orientation that have less than 8% plasma variations. It may prove easier to accept larger plasma variations; the effect of widening the criteria to 12% or 16% raises the required number of acceptable shots for a 5σ result to 11 or 18 in each spin orientation, respectively. For reference, DIII-D is capable of generating about 30 plasma shots per day, so this does not appear formidable.

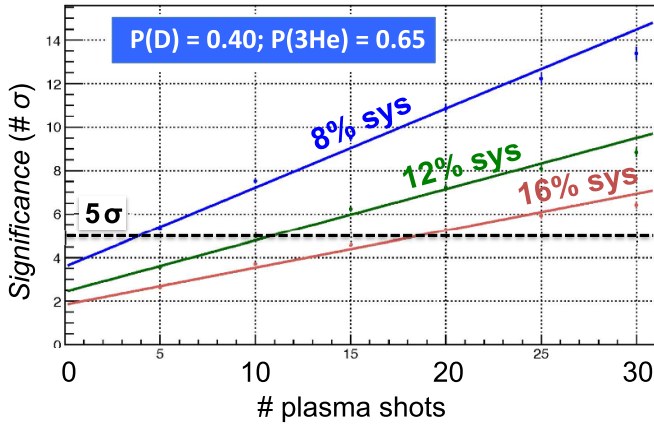
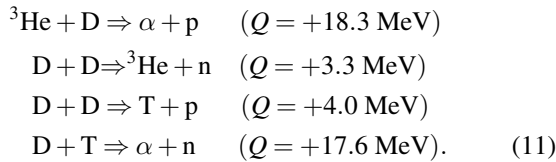


Figure 19. The number of plasma shots required to reach a given confidence level in terms of the statistical significance (σ), for different assumptions on the systematic shot-to-shot variations, as reflected in their fusion yields. The 5σ level for a definitive demonstration is indicated as the black dashed line.

6.2.4. Backgrounds from secondary reactions. In a $D + {}^3\text{He} \rightarrow \alpha + p$ polarization survival demonstration experiment, while a hydrogen plasma avoids diluting the spins of the injected reactants, nonetheless a chain of parallel and secondary reactions can also lead to the production of alphas and protons. These are listed with their associated energy release (Q values) in equation (11). Note that while triton production, followed by a subsequent $D + T$ reaction can generate an alpha of comparable energy to the $D + {}^3\text{He} \rightarrow \alpha + p$ fusion channel, the only secondary protons that are produced are low in energy and easily distinguished from those of the initial $D + {}^3\text{He} \rightarrow \alpha + p$ process.



In principle, a dilution of the signal of interest can come from a two-step burn-up process [97], in which an initial reaction of two polarized deuterons produces a ${}^3\text{He}$, the second process of equation (11), with some transferred polarization that is less than that of the initial ${}^3\text{He}$ pellet and not generally aligned with the local field. However, the rate of the primary ${}^3\text{He} + D$ reaction providing the *signal* is simply proportional to the number of deuterons, $n(D)$, and for a hydrogen plasma, the density $n(D)$ is just determined by the injected polarized fuel. The rate of the $D + D$ reactions producing ${}^3\text{He}$ is proportional to $n(D)^2$, and the rate of the subsequent ${}^3\text{He} + D$ burn-up process is proportional to $n(D)$. Thus, the dilution of the signal of interest by the two-step burn-up process is quenched by the factor $n(D)/n(D)^3$, and so is essentially negligible.

7. Summary

Spin-polarized fuels can increase fusion reactivity by up to 50% and provide a significant boost towards the ignition of

a burning plasma. In large-scale tokamaks, a further boost in power from increased alpha heating would accompany such gains. In the light of ITER simulations, it now seems quite likely that fuel polarization would survive through fuel burnup and have a major impact on performance (sections 3 and 4). A recent revolution in high-power lasers, combined with new molecular physics techniques, projects the capability of producing \sim fully polarized D and T in the quantities needed for a fusion power reactor (section 5.1.3 and appendix D). A necessary precursor to the research and development of such a capability is the crucial *in situ* demonstration of polarization survival in a high- T_{ion} H plasma, and we have studied the key steps needed to execute such an experiment.

An experiment to test polarization survival can be carried out using the $D + {}^3\text{He} \rightarrow \alpha + p$ reaction, avoiding the complications of handling tritium (section 2). There have been significant developments in polarized materials over the last several decades, driven by NP and by medical imaging. While their goals have been very different (e.g. few mole samples with lifetimes of 10^5 – 10^8 s, whereas several kmols per day would be needed to fuel a power reactor, but with mere ~ 10 s lifetimes), these existing techniques can be adapted to demonstrate an in-plasma spin enhancement in a cost-effective way. We have evaluated two options for preparing polarized deuterium, ${}^7\text{Li}$ D dynamically polarized to $P_V^D = 70\%$ (section 5.1.1) and frozen-spin H D polarized to $P_V^D = 40\%$ (section 5.1.2). To deliver polarized deuterium, ${}^7\text{Li}$ D would require an 0.2–0.3 K polarizer that could transfer pellets to a nearby ~ 2 K injection gun; H D could be encapsulated in thin ICF shells, pre-polarized in another facility and loaded into a similar ~ 2 K injection gun. We have mapped out the characteristics of GDP shells as a potential method of containing both H D and ${}^3\text{He}$ (section 5.1.2 and appendix C). ${}^3\text{He}$ gas can be pre-polarized by laser optical pumping methods and then diffused into GDP shells. Leveraging advances in medical imaging, ${}^3\text{He}$ polarization loss during shell diffusion loading has been found to be relatively small (section 5.2.1), and the polarization lifetime at 77 K unexpectedly long (section 5.2.2). GDP shells of ${}^3\text{He}$ can be prepared with 65% polarization and delivered to a plasma with a ~ 77 K injection gun. For the practical realization of such an experiment on DIII-D, a dedicated cryo-gun could be constructed to accommodate the injection of both polarized D and polarized ${}^3\text{He}$ through a vertical port (section 5.3).

Polarization survival experiments require a high T_{ion} hydrogen plasma to avoid dilution of the polarization of injected deuterium (section 6), and a campaign to develop this capability is in preparation. With polarized fuels injected into such a plasma, energetic protons (~ 15 MeV) detected at the plasma-facing wall would provide a nearly background-free monitor of $D + {}^3\text{He}$ fusion (section 6.2). The ratio of expected proton yields from successive plasma shots with D and ${}^3\text{He}$ spins parallel and anti-parallel range from 1.3 ($\text{HD} + {}^3\text{He}$) to 1.6 (${}^7\text{Li D} + {}^3\text{He}$). SPF Simulations have been carried out, and detailed tracking of fusion products confirms that this large enhancement is expected over a wide range of poloidal angles (section 6.2). By correlating existing DIII-D plasma diagnostics with fusion rates from unpolarized D

and ^3He , comparable plasma conditions could be selected to compare fusion yields from injected fuels with different spin alignments.

Acknowledgments

This work has been supported in part by the United States Department of Energy, Office of Nuclear Physics under Contract DE-AC05-06OR23177 through which Jefferson Science Associates operates Jefferson Laboratory. Some material is based upon work supported by the U.S. Department of Energy, Office of Fusion Energy Sciences, using the DIII-D National Fusion Facility, a DOE Office of Science user facility, under Award DE-FC02-04ER54698, and DIII-D users at the University of California at Irvine under Award DE-SC0020337. Support has also been provided by Internal Research and Development Funding from General Atomics, and in part by a grant from the University of Virginia Research and Initiative Fund. We thank G.M. Hale of LANL for carrying out the R-matrix analysis discussed in section 2. We thank F. Bombarda of ENEA-Frascati for raising the potential issue that we address in section 4.1. We are indebted to M. Farrell, M. Hoppe and M. Schoff of General Atomics for supplying ICF pellets for the test experiments described in section 5, and to F. Li for her assistance with measurements of pellet dimensions at Old Dominion University. We thank T.P. Rakitzis of the University of Crete for many fruitful discussions on the potential for a new generation of laser-driven polarized sources (section 5.1.3 and appendix D), M. Lanctot and H. St-John of General Atomics for their assistance with the ONETWO code used in the simulations of section 6.2, and C. Hanretty of Jefferson Lab for help with the Monte Carlo simulations shown in figure 19.

Disclaimer

This report was prepared as an account of work sponsored by an agency of the United States Government. Neither the United States Government nor any agency thereof, nor any of their employees, makes any warranty, express or implied, or assumes any legal liability or responsibility for the accuracy, completeness, or usefulness of any information, apparatus, product, or process disclosed, or represents that its use would not infringe privately owned rights. Reference herein to any specific commercial product, process, or service by trade name, trademark, manufacturer, or otherwise does not necessarily constitute or imply its endorsement, recommendation, or favoring by the United States Government or any agency thereof. The views and opinions of authors expressed herein do not necessarily state or reflect those of the United States Government or any agency thereof.

Appendix A. The D + ^3He fusion angular distributions in their center of momentum frame

In the center-of-momentum frame ($P_{\text{total}} = 0$), the natural quantization axis is the local magnetic field direction, along which the approaching deuterium and ^3He spins will align,

regardless of the angles of their initial-state momenta relative to the field direction. The reaction kinematics is shown schematically in figure A1.

We calculate the angular dependence of the cross section for α - p decay through the 16.9 MeV spin $3/2^+$ fusion resonance in ^5Li . With a Wigner-Eckart factorization, the reaction amplitude decomposes into a product of a reduced matrix element for fusion into the ^5Li intermediate state, a vector coupling (*Clebsch-Gordon*) coefficient for combining the D and ^3He spins along their initial quantization direction (\hat{z} in figure A1), another vector coefficient for coupling the final state spins along the α - p axis (\hat{z}'), and a Wigner $d_{m,m'}^J$ matrix element for the rotation between the two axes. Since the α has zero spin, to conserve parity and angular momentum, the α - p pair emerge from the spin (parity) $3/2$ (+) compound state with two units of orbital angular momentum (*D-wave*, perpendicular to their momenta), as in figure 2. The cross section is then the squares of amplitudes, summed over allowed final states.

The cross section with D and ^3He spins both parallel (*P*) to the local field is then evaluated as,

$$\begin{aligned} \frac{d\sigma^P}{d\Omega} &= |\langle f || T_{fi} || i \rangle|^2 \cdot \left| \left\langle 1+1; \frac{1}{2} + \frac{1}{2} \left| \frac{3}{2} \frac{3}{2} \right\rangle \right|^2 \right. \\ &\quad \cdot \left\{ \left| \left\langle 20; \frac{1}{2} + \frac{1}{2} \left| \frac{3}{2} + \frac{1}{2} \right\rangle \right|^2 \cdot |d_{3/2, +1/2}^{J=3/2}|^2 \right. \right. \\ &\quad \left. \left. + \left| \left\langle 20; \frac{1}{2} - \frac{1}{2} \left| \frac{3}{2} - \frac{1}{2} \right\rangle \right|^2 \cdot |d_{3/2, -1/2}^{J=3/2}|^2 \right\} \right. \\ &= |\langle f || T_{fi} || i \rangle|^2 \cdot \frac{2}{15} \cdot \left[\frac{9}{4} \sin^2 \theta \right]. \end{aligned}$$

Similarly, when the *D* and ^3He spins are anti-aligned (*A*) relative to the local field,

$$\begin{aligned} \frac{d\sigma^A}{d\Omega} &= |\langle f || T_{fi} || i \rangle|^2 \cdot \left| \left\langle 1+1; \frac{1}{2} - \frac{1}{2} \left| \frac{3}{2} \frac{1}{2} \right\rangle \right|^2 \right. \\ &\quad \cdot \left\{ \left| \left\langle 20; \frac{1}{2} + \frac{1}{2} \left| \frac{3}{2} + \frac{1}{2} \right\rangle \right|^2 \cdot |d_{1/2, +1/2}^{J=3/2}|^2 \right. \right. \\ &\quad \left. \left. + \left| \left\langle 20; \frac{1}{2} - \frac{1}{2} \left| \frac{3}{2} - \frac{1}{2} \right\rangle \right|^2 \cdot |d_{1/2, -1/2}^{J=3/2}|^2 \right\} \right. \\ &= |\langle f || T_{fi} || i \rangle|^2 \cdot \frac{2}{15} \cdot \left[\frac{1}{4} (1 + 3\cos^2 \theta) \right]. \end{aligned}$$

The unpolarized cross section for this reaction is isotropic, and can be constructed by averaging over all possible initial spin states. From this, the reduced matrix element can be recast as,

$$|\langle f || T_{fi} || i \rangle|^2 \cdot \frac{2}{15} = \left(\frac{d\sigma}{d\Omega} \right)_0.$$

Thus, the angular distributions with initial-state spins parallel and anti-aligned to the local field become,

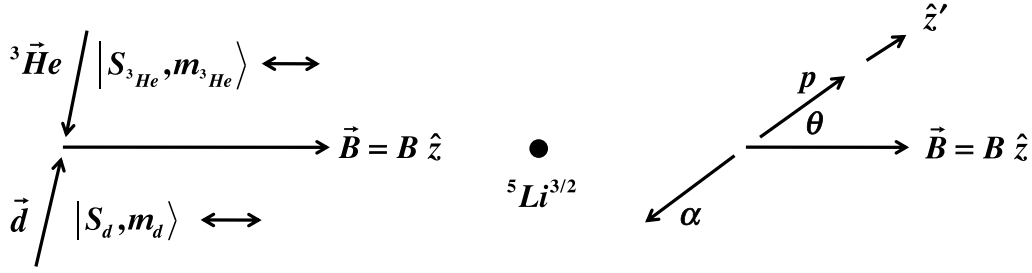


Figure A1. The initial (left) and final (right) states of the $D + {}^3\text{He}$ fusion reaction through a ${}^5\text{Li}$ compound state.

$$\frac{d\sigma^P}{d\Omega} = \left(\frac{d\sigma}{d\Omega} \right)_0 \cdot \frac{9}{4} \cdot \sin^2\theta,$$

$$\frac{d\sigma^A}{d\Omega} = \left(\frac{d\sigma}{d\Omega} \right)_0 \cdot \frac{1}{4} \cdot (1 + 3\cos^2\theta),$$

which are the curves shown in figure 4. The full angular dependence given in equation (3) can be derived in a similar manner. Thus, the highly anisotropic angular distributions that accompany the fusion of polarized fuel are a simple consequence of angular momentum and parity conservation.

Appendix B. Hyperfine splitting in singly-ionized ${}^3\text{He}^+$

The neutral ground state of ${}^3\text{He}$ has two electrons paired in a zero-spin $1s$ state with no net effect on the nucleus. Following fuel injection, a plasma collision quickly strips away one electron, and the system is then a ${}^3\text{He}^+$ ion with a hydrogen-atom-like state structure. The ion is left in one of four Zeeman states with a probability determined by the polarization prior to ionization. Two of the states have parallel electron and nuclear spins and are eigenstates of the system, but the two anti-parallel spin states are not. We can express the remaining two ion eigenstates in the Zeeman basis,

$$|2\rangle = a|+-\rangle - b|-+\rangle$$

$$|3\rangle = b|+-\rangle + a|-+\rangle,$$

where the Zeeman basis states are labeled by the sign of the m -value for the electron and the nucleus, respectively. The numbering of the eigenstates refers to the Zeeman energies of the states where $|1\rangle$ has the highest Zeeman energy. (The HFI shifts $|2\rangle$ to a slightly higher energy, as in figure B1.) The constants a and b are determined from the eigenvectors of the 4×4 Hamiltonian matrix of the combined HFI, $H_{\text{HFI}} = A_{\text{HFI}} \vec{I}_{\text{ion}} \cdot \vec{S}_e$, and the Zeeman interaction, $H_{\text{Zeeman}} = -(\vec{\mu}_{\text{ion}} + \vec{\mu}_e) \cdot \vec{B}$. They are normalized so that $a^2 + b^2 = 1$. The explicit solutions for a and b are,

$$a^2 = \frac{D^2}{A_{\text{HFI}}^2 + D^2}, \text{ and } b^2 = \frac{A_{\text{HFI}}^2}{A_{\text{HFI}}^2 + D^2},$$

where $D = \sqrt{A_{\text{HFI}}^2 + 4(\mu_{\text{ion}} - \mu_e)^2 B^2} + 2(\mu_{\text{ion}} - \mu_e)B$. The four eigenenergies are plotted in figure B1 as a function of the external magnetic field, using values from the most recent experimental determination of A_{HFI} for the ${}^3\text{He}^+$ ion [51].

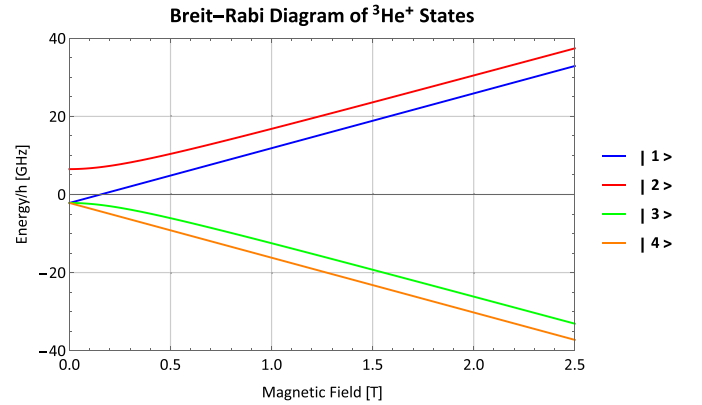


Figure B1. The energies of the four eigenstates of ${}^3\text{He}^+$ versus magnetic field. (See text for state labeling. For scale reference, $24 \text{ GHz} \equiv 0.1 \text{ meV}$.) Above ~ 1 tesla, electron Zeeman energy dominates, splitting the states into two pairs. The hyperfine interaction further splits each pair so that the spin anti-parallel member of each pair is slightly higher in energy. The Zeeman energy of the nucleus is not discernable on this scale.

The previous expressions for $|2\rangle$ and $|3\rangle$ can be used to express the Zeeman basis states in terms of the ion eigenstates, as shown in column 2 of table B1, where the phase difference, $\phi(t) = \Delta Et/\hbar$, that develops over time between the two eigenstates has been included as well. In column 3 is given the expectation value of the nuclear polarization, $\langle |P| \rangle = \langle |m_{\text{ion}}/I_{\text{ion}}| \rangle$, for each of the states as a function of time. As evident in figure B1, the energy difference is in the range of multi-GHz while the second ionization is expected to occur on a time scale of micro-seconds. Thus, $\cos(\phi)$ will be randomly distributed and drop out in the ensemble average. Column 4 of table B1 is the fraction of the ensemble in each state for an initial nuclear polarization P_i .

Taking the ensemble average of the entries in column 3 of table B1 (so that $\langle \cos \phi \rangle = 0$), multiplying by column 4, and summing over final states, we arrive at the final polarization, P_f ,

$$P_f = P_i \cdot \frac{1 + (a^2 - b^2)^2}{2}.$$

The fraction of the initial polarization that is lost is then, $(P_i - P_f)/P_i = \frac{1}{2} \left\{ 1 - (a^2 - b^2)^2 \right\} = 2a^2b^2$.

Table B1. The states of $^3\text{He}^+$ and their polarization factors. The Zeeman basis are labeled by the sign of the m-value for the electron and the nucleus, respectively.

Zeeman state	Ion eigenstate representation	Polarization = $\langle P \rangle$	Ensemble fraction
$ ++\rangle$	$ 1\rangle$	1	$\frac{1}{4}(1 + P_i)$
$ +-\rangle$	$a 2\rangle + be^{i\phi} 3\rangle$	$-(a^2 - b^2)^2 - 4a^2b^2\cos\phi$	$\frac{1}{4}(1 - P_i)$
$ --\rangle$	$-be^{-i\phi} 2\rangle + a 3\rangle$	$+(a^2 - b^2)^2 + 4a^2b^2\cos\phi$	$\frac{1}{4}(1 + P_i)$
$ ---\rangle$	$ 4\rangle$	-1	$\frac{1}{4}(1 - P_i)$

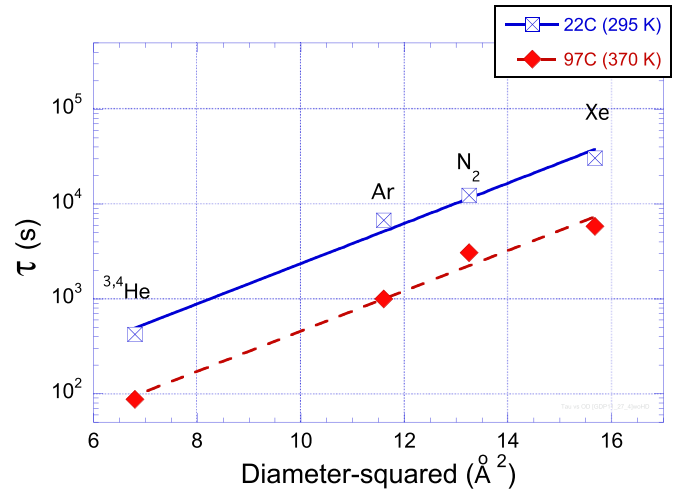
In terms of the relevant parameters this becomes,

$$\frac{P_{\text{lost}}}{P} = \frac{1}{2} \left[1 + \frac{4(\mu_e - \mu_{\text{ion}})^2}{A_{\text{HFI}}^2} B^2 \right]^{-1}. \quad (\text{B1})$$

Appendix C. Permeation characteristics of GDP shells

The GDP shell material is commonly used in ICF experiments. Spheres are manufactured by vapor deposition onto the surface of poly-alpha-methylstyrene (PAMS) mandrels in a plasma of Trans-2 Butene and Hydrogen. Subsequent heating and pumping on the spheres removes the PAMS material, which permeates out and leaves behind a thin GDP shell comprised of a cross-linked structure of Carbon and Hydrogen. The C:H ratio can vary between 0.68 and 1.16, and higher values are associated with a higher Young's elastic modulus, making them more robust. Shells studied at JLab are typical of *standard* GDP shells, with C:H ~ 0.85 and density 1.04 g cc^{-1} ; these are the values used in the calculations of the extraneous particle numbers given in table 2. The mechanical properties of GDP shells have been thoroughly investigated [20]. Their permeation characteristics relevant to this application have been studied at Jefferson Lab. Thin-walled shells are filled by controlling the temperature-dependent permeation rate. Initially, they are evacuated at room temperature by simply pumping on their storage container. The characteristic time constant (τ) when permeating an external pressure P_0 into an evacuated shell, $P_{\text{GDP}} = P_0(1 - e^{-t/\tau})$, depends linearly on shell dimensions, inversely on temperature and on a chemical permeation coefficient, $\tau = Dw/(6K_pRT)$ [98, 99]. Here D is the diameter of the shell and w the wall thickness, the gas constant R is $8.314 \text{ m}^3 \text{ Pa mol}^{-1} \text{ K}^{-1}$, T is the temperature in Kelvin, and K_p is a permeation coefficient with an Arrhenius-type temperature-dependence, $K_p = K_0 \cdot \exp(-\varepsilon_p/k_B T)$, expressed in units of $\text{mol}/(\text{m}\cdot\text{Pa}\cdot\text{s})$, with a chemical activation energy ε_p (eV).

Sample pellets of about 2 mm diameter, with wall thicknesses between 16 and $29 \mu\text{m}$ s, were supplied to JLab by GA. Precise measurements of pellet diameter and wall thickness were obtained, using facilities at *Old Dominion University*, by counting the interference fringes created when 546 nm monochromatic light passed through the pellet walls [100, 101].

**Figure C1.** Permeation time constants measured at JLab for different gases in a 1.9 mm OD GDP pellet with a $29 \mu\text{m}$ wall thickness, at room temperature and at 97 C. (Statistical uncertainties are smaller than the symbols.)

Permeation measurements were carried out on a single pellet at a time. Each pellet was prepared at room temperature by evacuation within a small storage container, a stainless-steel tube with a 4 mm inside-diameter, and then filled with the gas of interest, allowing many permeation time constants at both steps. The measurements of permeation rates were then carried out following a sudden evacuation of the storage tube, to drop the pressure outside the pellet, and then subsequent monitoring of the rate of gas evolving with time from the container through either a Residual Gas Analyzer (RGA) or a leak detector (for gases of mass 3 or 4). Permeation measurements at elevated temperatures were carried out with the storage tube immersed in heated oil; for measurements at 273 K or 195 K the storage tube was immersed in baths of ice water or dry ice, respectively. The pressure from the gas permeating through the pellet wall ($\sim \text{mb}$) was sufficient to maintain thermal equilibrium with the thermal bath.

As an example, the permeation rates measured through the $29 \mu\text{m}$ thick wall of a 1.9 mm diameter GDP pellet are plotted in figure C1 as a function of the square of the kinetic diameter of the gas species. Permeation is limited by the mean-free path in the material, which is in turn related to the cross-sectional area of the gas atom/molecule. This leads to a

simple exponential dependence, $\exp(D^2/\alpha)$ where $\alpha \sim 2$ when D is expressed in Angstroms (e.g. for the fits in figure C1, $\alpha = 2.045$). A change in temperature of the thermal bath by 75 degrees (C or K) leads to a parallel shift in permeation rates of all gases by a factor of 5. The permeation rates for the species relevant to the fusion experiment, with wall thicknesses ranging from 16 to 29 μm , are shown in figure 9 of section 5.1 over a larger temperature range. From the fit to those data (the dotted line in figure 9), the permeation coefficient is determined as $K_0 = 3.34 \pm 0.51 \times 10^{-12} \text{ mol (m s Pa)}^{-1}$, with activation energy $\varepsilon_p = 0.148 \pm 0.005 \text{ eV}$.

Appendix D. High-flux laser-driven polarized \vec{D}

There are several versions of this general scheme [102–107]. We sketch one that is described in [107] that can capitalize on new laser developments and yield fully polarized sources of D, T or DT [108].

- (i) As a source material, we consider a gaseous deuterated (and tritiated) formaldehyde, $CDTO$, $CHDO$ or CD_2O , where only the hydrogen isotopes carry nuclear spin. The gas is expanded through a nozzle, and the cooling from expansion drives most of the molecules into their ground state with J (rotational) = 0, $m_J = 0$, ν (vibrational) = 0. The molecules exit the nozzle with a rather well-defined velocity of about 2 km s⁻¹.
- (ii) The molecular beam then passes through two circularly polarized IR laser beams, fired perpendicular to the propagation direction. Through coherent Raman scattering (*Stimulated Raman Adiabatic Passage*, or STIRAP) they pump the molecule into a ro-vibrational excited state with two units of rotational angular momentum, $J = 2$ and $m_J = +2$.
- (iii) The hyperfine (HF) interaction between the rotational angular momentum and the spins of the hydrogen isotopes splits the m_J levels. As the system evolves, the total angular momentum beats between rotational and nuclear spins, and the population of the fully nuclear polarized state ($m_J = -1$ for DT, or $m_J = -2$ for D₂) increases. Significant population (20%) in this fully polarized state is achieved after about 10 μs .
- (iv) The beating rate between the nuclear and orbital spins allows time for the molecular beam to travel from the gas expansion nozzle to a region with a modest field (a few milli-tesla) that stops the hyperfine beating at a point when the population in the state with full nuclear polarization is large.
- (v) Within the field region, another IR laser transition selects the hyperfine level with full nuclear polarization and pumps it to a $J = 1$, $m_J = +1$ state of DT (or to $J = 0$ for D₂). This state is exclusively photo-dissociated with a high-resolution visible laser, tuned so that only the state with full nuclear polarization has sufficient energy to dissociate. The dissociating laser line can be chosen to break the bond of interest, so as to yield CO + DT (or COH + D, etc.), depending on the source gas.

- (vi) The dissociation region ends within a larger field magnet (~ 1 tesla), which prevents hyperfine beating in the separated isotopic hydrogen atoms between electrons and their polarized nuclei. The molecular rotational angular momentum $J = 1$, created by the IR excitations in the previous step, also aligns the molecular bonds, since the orbital angular momentum J and the bonds are always perpendicular. As a result, the polarized fragments will be emitted with a CM angular distribution that is highly peaked perpendicular to the initial nozzle-expansion momentum. After dissociation, the polarized DT (or D) carry almost all of the kinetic energy. If the preceding stages are arranged vertically, the dissociated CO (or COH) fragments will continue to drift downward, while the polarized hydrogen-like atoms emerge highly peaked horizontally.

The result of the previous steps is an intense source of highly polarized DT molecules (or D atoms) with $\sim 100\%$ nuclear polarizations [107]. It would be relatively straightforward to collect and freeze these in open-ended capsules cooled to $\sim 2 \text{ K}$, which could then be transferred to a cryogenic pellet injector.

Most of these steps have already been demonstrated, although only at relatively low powers. Commercial table-top, tunable, narrow band-width lasers should produce polarized fluxes of 10^{21} s^{-1} . Industrial scale lasers could exceed fluxes of 10^{22} s^{-1} with nearly 100% polarization [108]. With such capabilities, scenarios for fueling a tokamak power reactor with polarized fuel become realistic. Nonetheless, as with any new technique that jumps previous boundaries by many orders of magnitude, focused research and development will be necessary to demonstrate the predicted flux scaling. The driving factor for such research is a demonstration of polarization survival in a realistic plasma.

Appendix E. MRI imaging of polarized ^3He shells

MRI relies on pulsed NMR in which nuclear spins, aligned along a static magnetic field, B_0 , are subjected to pulses of an RF magnetic field, B_1 , transverse to B_0 , and oscillating at the nominal Larmor frequency $f_0 = \gamma B_0/2\pi$, where $\gamma/2$ is the gyromagnetic ratio ($-32.434 \text{ MHz/tesla}$ for ^3He). Viewed semi-classically, an *excitation* RF pulse of flip angle θ tips a fraction $(1 - \cos \theta)$ of the aligned spins into the transverse plane. The transverse spins then precess about B_0 at the local Larmor frequency. The rotating magnetic field generated by the magnetic moments of the precessing spins induces an oscillating current in a surrounding RF receiver coil, which constitutes the NMR signal.

The amplitude for a signal generated by an RF excitation pulse, often referred to as the *Free Induction Decay* (FID), follows a decaying exponential of the general form, $S(t) = Ae^{i\phi} e^{-i2\pi(f-f_0)t} e^{-t/T_2^*}$. Here, f is the local resonance frequency, which can deviate from the Larmor frequency (f_0) due to chemical shifts induced by molecular bonds in surrounding material (or stray magnetic fields, if any), and T_2^* is the

transverse spin relaxation time due to interactions with neighboring spins and local field inhomogeneities. If the sample contains more than one distinct spin population, each with its unique resonance frequency f_k , then the total signal is the coherent sum of multiple decaying exponentials, each with their own amplitude, phase offset, and transverse decay time. The frequency content of the FID can be resolved by taking the Fourier transform of the NMR signal. When the FID is a sum of decaying complex exponential functions, then its Fourier transform is a sum of complex Lorentzians.

Spatial localization in MRI is achieved by applying magnetic field gradients across the sample. The gradients, superimposed on B_0 , cause the z component of the magnetic field to vary linearly along orthogonal directions, and this in turn causes the Larmor frequency to vary along those direction. Imaging data is acquired with an MRI *pulse sequence*—a prescribed series of RF pulses, magnetic field gradients, and data-sampling windows. These sequences use the linear mapping between frequency and position created by the applied gradients to encode spatial information about the excited spins into the frequency and/or phase of the NMR signal [109]. Signal data acquired in this manner are organized in terms of their Fourier-transformed coordinates—their ' k space'. For a study of polarization within 2 mm shells, we require half-millimeter imaging resolution, and for polarized gas this can be challenging. (Note that this is about an order of magnitude finer resolution than is typical of medical imaging with polarized gases.) We have achieved this with (fully *phase encoded*) pulse sequences that sample a single element of the k -space data matrix following each excitation RF pulse [79, 80]. This takes advantage of the extremely long transverse decay time ($T_2^* \sim 100$ ms) inside a hollow container [110], making it practical to enhance the signal-to-noise by longer signal readout times without decrementing polarization (i.e. with low flip angle). Nonetheless, data over the entire field of view must be acquired to evaluate the k -space matrix. It is for this reason that the ^3He volume to be imaged is restricted to the small tubes of figure 10. This keeps the total time required for DAQ down to a manageable fraction of the pellet wall diffusion time so that the pellet permeation process can be directly observed.

The same pulse sequence can provide both spatial and spectral information. Applying a discrete inverse Fourier transform along the spatial dimensions transforms the k -space data into image space, and applying the Fourier transform along the temporal dimension yields the frequency spectrum of all transverse spins contained in each image pixel. The results are termed *Chemical Shift Images* (CSI), since discrete spin populations resulting from local magnetic field perturbations from chemical bond differences can be separated in frequency.

Immersing a uniform sphere in an otherwise uniform magnetic field creates a dipole-shaped field perturbation outside the sphere, whose overall magnitude scales with the magnetic susceptibility difference between the sphere and the surrounding medium [79]. This is the role of a solid glass bead positioned immediately beneath the GDP pellet, as evident in figure 10. The local magnetic field perturbation due to the nonzero magnetic susceptibility of the glass bead causes a small but prominent magnetic field shift inside the adjacent

GDP pellet, and this allows the signal inside and outside the pellet to be tracked separately using spectrally sensitive CSI acquisition. (In fact, no such frequency separation is observed in experiments performed without the presence of a glass bead.)

Considering figure 11, all image voxels contain a spectral peak centered within a few Hz of the scanner's Larmor frequency, f_0 . However, image voxels overlapping the location of the pellet also contain another prominent peak centered ~ 30 Hz above f_0 . Because the ^3He diffusion length during the acquisition time exceeds the bead diameter, each spin can experience a wide range of frequency shifts across all voxels located within several millimeters of the glass bead. In contrast, the range of frequency shifts experienced by spins within the pellet is considerably narrower, because the pellet walls confine the encapsulated spins to a limited region of the dipole-shaped field perturbation. As a result, the NMR response of spins inside the pellet appears in a well-defined peak that is shifted in frequency [79, 80]. Thus, the frequency shifts resulting from the presence of the glass bead allow the NMR signal from spins located inside and outside the pellet to be tracked independently, providing separate time evolutions of each.

Appendix F. Orbit Tracking in DIII-D

The calculation for the flux of lost charged fusion products reaching the vessel wall consists of the following steps.

- (1) Calculate the number of fusion reactions, F , as a function of major radius and elevation, $F = F(R_{\text{birth}}, z_{\text{birth}})$, where F is in units of particles/s. A radial profile of F is output by the ONETWO power balance code [91, 92], and then distributed across a two-dimensional spatial grid in major radius and elevation to determine the particle starting locations.
- (2) For each birth location featuring a non-zero fusion reaction rate, the number of fusion reactions is distributed across pitch angle and gyrophase:
 - 13 values of pitch angle, $0^\circ \leq \theta \leq 180^\circ$, including $v_{\parallel}/v = \pm 1$,
 - 12 values of gyrophase, excluding $v_{\parallel}/v = \pm 1$ (for which the gyrophase is singular).

An orbit is then calculated for each of these pitch angle and gyrophase pairs at each position ($R_{\text{birth}}, z_{\text{birth}}$). This is performed as the second step because identifying the values of ($R_{\text{birth}}, z_{\text{birth}}$) with non-zero fusion rate greatly reduces the number of orbits to be calculated.

- (3) The orbit of each particle in (2) is calculated for 5000 steps with a 1 cm step size. If the particle does not hit the wall within 5000 steps, then it is considered to be confined. That number of steps is determined empirically and is considered reasonable because the large orbit scale of these high energy ions results in them reaching the wall very quickly unless their full orbit is confined (which is itself a very rare occurrence).
- (4) In practice, with the discretization of step (2), each wall strike location originates from a unique birth location

($R_{\text{birth}}, z_{\text{birth}}$) with a specific choice of (pitch, gyrophase) angles. The particle flux at that wall location is determined by scaling the fusion rate $F = F(R_{\text{birth}}, z_{\text{birth}})$ from step (1) by the fraction of fusion products emitted into that (θ pitch, $\phi =$ gyrophase) bin, weighted by phase space, for the assumed degrees of fuel polarization, as determined by W in equation (4),

$$F'(R_{\text{birth}}, z_{\text{birth}}, \theta, \phi) = (1/4\pi)W_A(\theta) \sin(\theta) (\Delta\theta = \pi/13)(\Delta\phi = 2\pi/12)F(R_{\text{birth}}, z_{\text{birth}}).$$

- (5) Wall strikes are then histogrammed by binning the wall in segments of 0.01 m^2 in area (A). The particle count is reduced by a factor $2\pi R_i A$, where R_i is the major radius at the center of each wall segment, to account for the axisymmetry of the loss pattern. The end result is a particle flux density as a function of poloidal position along the wall, such as in figure 17.

ORCID iDs

A. Deur  <https://orcid.org/0000-0002-2203-7723>

N. Eidietis  <https://orcid.org/0000-0003-0167-5053>

W.W. Heidbrink  <https://orcid.org/0000-0002-6942-8043>

A.M. Sandorfi  <https://orcid.org/0000-0001-8309-8581>

References

- [1] Conner J.P., Bonner T.W. and Smith J.R. 1952 A study of the $\text{H}^3(\text{d}, \text{n})\text{He}^4$ reaction *Phys. Rev.* **88** 468
- [2] Bonner T.W., Conner J.P. and Lillie A.B. 1952 Cross Section and Angular Distribution of the $\text{He}^3(\text{d}, \text{p})\text{He}^4$ Nuclear Reaction *Phys. Rev.* **88** 473
- [3] Goldhaber M. 1934 On the probability of artificial nuclear transformations and its connection with the vector model of the nucleus *Math. Proc. Camb. Phil. Soc.* **30** 561
- [4] Kulsrud R.M., Furth H.P., Valeo E.J. and Goldhaber M. 1982 Fusion Reactor Plasmas with Polarized Nuclei *Phys. Rev. Lett.* **49** 1248
- [5] More R.M. 1983 Nuclear Spin-Polarized Fuel in Inertial Fusion *Phys. Rev. Lett.* **51** 396
- [6] Coppi B., Pegoraro F. and Ramos J.J. 1983 Instability of Fusing Plasmas and Spin-Depolarization Processes *Phys. Rev. Lett.* **51** 892
- [7] Lodder J.J. 1983 On the possibility of nuclear spin polarization in fusion reactor plasmas *Phys. Lett. A* **98** 179
- [8] Coppi B., Cowley S., Kulsrud R.M., Detragiache P. and Pegoraro F. 1986 High-energy components and collective modes in thermonuclear plasmas *Phys. Fluids* **29** 4060
- [9] Cowley S., Kulsrud R.M. and Valeo E.J. 1986 A kinetic equation for spin-polarized plasmas *Phys. Fluids* **29** 430
- [10] Kulsrud R.M., Valeo E.J. and Cowley S. 1986 Physics of spin-polarized plasmas *Nucl. Fusion* **26** 1443
- [11] Finn P., Brooks J., Ehst D., Gohar Y., Mattas R. and Baker C. 1985 An Evaluation of Polarized Fuels in a Commercial Deuterium/Tritium Tokamak Reactor ANL/FPP-85-1, Report DE86-007949 (available at: https://inis.iaea.org/collection/NCLCollectionStore/_Public/17/063/17063821.pdf?r=1)
- [12] Finn P., Brooks J., Ehst D., Gohar Y., Mattas R. and Baker C. 1986 An Evaluation of Polarized Fuels in a Commercial Deuterium/Tritium Tokamak Reactor *Fusion Sci. Technol.* **10** 902
- [13] Sandorfi A.M. and D'Angelo A. 2016 Prospects for Direct In Situ Tests of Polarization Survival in a Tokamak *Nuclear Fusion with Polarized Fuel (Springer Proceedings Physics vol 187)* ed G. Ciullo, R. Engels, M. Büscher and A. Vasilyev (Berlin: Springer) p 115
- [14] Crabb D.G. and Meyer W. 1997 Solid Polarized Targets for Nuclear and Particle Physics Experiments *Annu. Rev. Nucl. Part. Sci.* **47** 67
- [15] Goertz S., Meyer W. and Reicherz G. 2002 Polarized H, D and ^3He targets for particle physics experiments *Prog. Part. Nucl. Phys.* **49** 403
- [16] Bass C.D. et al 2014 A portable cryostat for the cold transfer of polarized solid HD targets: HDice-I *Nucl. Instrum. Methods Phys. Res. A* **737** 107
- [17] Kauczor H.U., Hofmann D., Kreitner K.F., Nilgens H., Surkau R., Heil W., Potthast A., Knopp M.V., Otten E.W. and Thelen M. 1996 Normal and abnormal pulmonary ventilation: visualization at hyperpolarized ^3He MR imaging *Radiology* **201** 564
- [18] Babcock E., Nelson I., Kadlecsek S., Driehuys B., Anderson L.W., Hersman F.W. and Walker T.G. 2003 Hybrid Spin-Exchange Optical Pumping of ^3He *Phys. Rev. Lett.* **91** 123003
- [19] Mooney K.E., Miller G.W., Dolph P.A., Tobias W.A., Nelyubin V., Singh J., Mugler-III J.P. and Cates G.D. 2009 A 3-Liter Capacity, Hybrid Spin-Exchange ^3He Polarizer for Medical Imaging *Proc. Soc. Magn. Reson. Med.* **17** 2166 (available at: <https://cds.ismrm.org/protected/09MProceedings/PDFfiles/02166.pdf>)
- [20] Nikroo A., Czechowicz D., Chen K., Dicken M., Morris C., Andrews R., Greenwood A. and Castillo E. 2004 Mechanical Properties of Thin GDP Shells Used as Cryogenic Direct Drive Targets at OMEGA *Fusion Sci. Technol.* **45** 229
- [21] Baylor L.R., Jernigan T.C., Parks P.B., Antar G., Brooks N.H., Combs S.K., Fehling D.T., Foust C.R., Houlberg W.A. and Schmidt G.L. 2007 Comparison of deuterium pellet injection from different locations on the DIII-D tokamak *Nucl. Fusion* **47** 1598
- [22] Sandorfi A.M. et al 2017 Polarized fusion, its Implications and plans for Direct Measurements in a Tokamak *22nd International Spin Symposium (SPIN'16) (University of Illinois, Urbana Illinois, 25–30 September 2016)* (available at: <https://arxiv.org/pdf/1703.06165.pdf>)
- [23] Paetz Gen Schieck H. 2016 Spin Physics and Polarized Fusion: Where We Stand *Nuclear Fusion with Polarized Fuel (Springer Proceedings Physics vol 187)* ed G. Ciullo, R. Engels, M. Büscher and A. Vasilyev (Berlin: Springer) p 15
- [24] Andreyanov A. et al 2021 Study of $^2\text{H}(\text{d}, \text{p})^3\text{H}$ and $^2\text{H}(\text{d}, \text{n})^3\text{He}$ Nuclear Reactions with Polarized Deuteron Beams. PolFusion Experiment *Phys. At. Nucl.* **84** 1895
- [25] Pace D.C., Lancot M.J., Jackson G.L., Sandorfi A.M., Smith S.P. and Wei X. 2016 Controlling Fusion Yield in Tokamaks with Spin Polarized Fuel, and Feasibility Studies on the DIII-D Tokamak *J. Fusion Energy* **35** 54
- [26] Garcia A.V., Heidbrink W.W. and Sandorfi A.M. 2023 Conceptual design of DIII-D experiments to diagnose the lifetime of spin polarized fuel *Nucl. Fusion* **63** 026030
- [27] Honig A. and Sandorfi A.M. 2007 Experimental test in a tokamak of fusion with spin-polarized D and ^3He *17th Int. Spin Physics Symposium (SPIN'06) AIP Conf. Proc. (Kyoto, Japan, 2–7 October 2006)* vol 915 p 1010
- [28] Smith S.P. et al 2018 The potential for retention of spin polarization to raise fusion reactivity *27th IAEA Fusion Energy Conf. Gandhinagar [FIP/P3-10]* (available at: <https://nucleus.iaea.org/sites/fusionportal/SharedDocuments/FEC2018/fec2018-preprints/preprint0290.pdf>)

- [29] Bosch H.S. and Hale G.M. 1992 Improved formulas for fusion cross-sections and thermal reactivities *Nucl. Fusion* **32** 611
- [30] Bahcall J.N. 1966 Non-Resonant Nuclear Reactions at Stellar Temperatures *Astrophys. J.* **143** 259
- [31] Tilley D.R. et al 2002 Energy levels of light nuclei $A=5, 6, 7$ *Nucl. Phys. A* **708** 3
- [32] Hale G.M. and Dodder D.C. 1980 R-Matrix analyses of light-element reactions for fusion applications *Int. Conf. on Nuclear Cross Sections for Technology (Univ. of Tennessee, Knoxville, TN USA, 22–26, October 1979)* ed Fowler J.L., Johnson C.H. and Bowman C.D. Nat. Bur. Stand. (USA) SP594, 650
- [33] Geist W.H., Brune C.R., Karwowski H.J., Ludwig E.J., Veal K.D. and Hale G.M. 1999 The $^3\text{He}(\rightarrow d,p)^4\text{He}$ reaction at low energies *Phys. Rev. C* **60** 054003
- [34] Lane A.M. and Thomas R.G. 1958 R-Matrix Theory of Nuclear Reactions *Rev. Mod. Phys.* **30** 257
- [35] Hale G. 2007 private communication (Los Alamos National Laboratory)
- [36] Leemann C.H., Bürgisser H., Huber P., Rohrer U., Paetz Gen Schieck H. and Seiler F. 1971 Investigation of the $^3\text{He}(d,p)^4\text{He}$ reaction with polarized beam and target at 430 keV *Ann. Phys.* **66** 810
- [37] Ohlsen G.G. 1972 Polarization transfer and spin correlation experiments in nuclear physics *Rep. Prog. Phys.* **35** 717
- [38] Conzett H.E. 1984 Spin-polarization observables at the $J = 3/2^+$ resonance in the reactions $^3\text{H}(d,n)^4\text{He}$ and $^3\text{He}(d,p)^4\text{He}$ *Proc. 10th Int. IUPAP Conf. on Few Body Problems in Physics (Karlsruhe, Germany 21–27 August 1983)* ed B Zeitnitz (Elsevier Science Publishing) p 539
- [39] Rekaló M.P. and Tomasi-Gustafsson E. 1998 Polarization phenomena for low energy $d+^3\text{He}$ collisions *Phys. Rev. C* **57** 2870
- [40] Rekaló M.P. and Tomasi-Gustafsson E. 2000 Nuclear processes in magnetic fusion reactors with polarized fuel arXiv:nucl-th/0010046
- [41] Aymar R., Barabaschi P. and Shimomura Y. 2002 The ITER design rep *Plasma Phys. Control. Fusion* **44** 519
- [42] Hawryluk R.J. 1981 An empirical approach to tokamak transport *Int. School of Plasma Physics, Varenna, Italy, Physics of Plasmas Close to Thermonuclear Conditions (August 1979)* ed B. Coppi, G.G. Leotta, D. Pfirsch, Pozzoli R. and E. Sindoni (Elsevier) vol 1 p 19 (available at: <https://transp.pppl.gov/biblio.html>)
- [43] Callen J.D. 1992 Transport processes in magnetically confined plasmas *Phys. Fluids B* **4** 2142
- [44] Hölzl M., Günter S., Classen I.G.J., Yu Q. and Delabie E. 2009 Determination of the heat diffusion anisotropy by comparing measured and simulated electron temperature profiles across magnetic islands *Nucl. Fusion* **49** 115009
- [45] Belli E.A. and Candy J. 2015 Neoclassical transport in toroidal plasmas with nonaxisymmetric flux surfaces *Plasma Phys. Control. Fusion* **57** 054012
- [46] Hazeltine R.D. 1973 Recursive derivation of drift-kinetic equation *Plasma Phys.* **15** 77
- [47] Staebler G.M., Kinsey J.E. and Waltz R.E. 2007 A theory-based transport model with comprehensive physics *Phys. Plasmas* **14** 055909
- [48] Candy J., Holland C., Waltz R.E., Fahey M.R. and Belli E. 2009 Tokamak profile prediction using direct gyrokinetic and neoclassical simulation *Phys. Plasmas* **16** 060704
- [49] Na Y.S., Kessel C.E. and Park J.M. 2008 Simulation of Hybrid Operation Modes in ITER *J. Korean Phys. Soc.* **53** 3788
- [50] Tiesinga E., Mohr P.J., Newell D.B. and Taylor B.N. 2021 CODATA recommended values of the fundamental physical constants: 2018 *Rev. Mod. Phys.* **93** 025010
- [51] Schneider A. et al 2022 Direct measurement of the $^3\text{He}^+$ magnetic moments *Nature* **606** 878
- [52] Lao L.L., St. John H.E., Peng Q., Ferron J.R., Strait E.J., Taylor T.S., Meyer W.H., Zhang C. and You K.I. 2005 MHD Equilibrium Reconstruction in the DIII-D Tokamak *Fusion Sci. Technol.* **48** 968
- [53] Burrell K.H., Kaplan D.H., Gohil P., Nilson D.G., Groebner R.J. and Thomas D.M. 2001 Improved charge coupled device detectors for the edge charge exchange spectroscopy system on the DIII-D tokamak *Rev. Sci. Instrum.* **72** 1028
- [54] Carlstrom T.N. et al 1992 Design and operation of the multipulse Thomson scattering diagnostic on DIII-D *Rev. Sci. Instrum.* **63** 4901
- [55] Schuessler H.A., Fortson E.N. and Dehmelt H.G. 1969 Hyperfine Structure of the Ground State of $^3\text{He}^+$ by the Ion-Storage Exchange-Collision Technique *Phys. Rev.* **187** 5
- [56] Crampton S.B., Kleppner D. and Ramsey N.F. 1963 Hyperfine Separation of Ground-State Atomic Hydrogen *Phys. Rev. Lett.* **11** 338
- [57] Wineland D.J. and Ramsey N.F. 1972 Atomic Deuterium Maser *Phys. Rev. A* **5** 821
- [58] Anderson L.W., Pipkin F.M. and Baird J.C. Jr 1960 Hyperfine Structure of Hydrogen, Deuterium, and Tritium *Phys. Rev.* **120** 1279
- [59] Bakalov D., Korobov V.I. and Schiller S. 2006 High-Precision Calculation of the Hyperfine Structure of the HD^+ Ion *Phys. Rev. Lett.* **97** 243001
- [60] Gatto R. 2016 Depolarization of Magnetically Confined Plasmas *Nuclear Fusion with Polarized Fuel (Springer Proceeding Physics vol 187)* ed G. Ciullo, R. Engels, M. Büscher and A. Vasilyev (Berlin: Springer) p 79
- [61] Garzotti L. et al 2012 Simulations of density profiles, pellet fuelling and density control in ITER *Nucl. Fusion* **52** 013002
- [62] Pacher G.W., Pacher H.D., Janeschitz G. and Kukushkin A S 2008 ITER operation window determined from mutually consistent core-SOL-divertor simulations: definition and application *Nucl. Fusion* **48** 105003
- [63] Greenside H.S., Budny R.V. and Post D.E. 1984 Depolarization of D–T plasmas by recycling in material walls *J. Vac. Sci. Technol. A* **2** 619
- [64] Jackson G.L. et al 1991 Regime of very high confinement in the boronized DIII-D tokamak *Phys. Rev. Lett.* **67** 3098
- [65] Jackson G.L. et al 1992 Very high confinement discharges in DIII-D after boronization *Phys. Fluids B* **4** 2181
- [66] Pace D.C., Heidbrink W.W. and Van Zeeland M. 2015 Keeping fusion plasmas hot *Phys. Today* **68** 34
- [67] Coppi B., Cowley S., Kulsrud R., Detragiache P. and Pegoraro F. 1986 High-energy components and collective modes in thermonuclear plasmas *Phys. Fluids* **29** 4060
- [68] McClements K.G., D’Inca R., Dendy R.O., Carbajal L., Chapman S.C., Cook J.W.S., Harvey R.W., Heidbrink W.W. and Pinches S.D. 2015 Fast particle-driven ion cyclotron emission (ICE) in tokamak plasmas and the case for an ICE diagnostic in ITER *Nucl. Fusion* **55** 043013
- [69] Thome K.E., Pace D.C., Pinsker R.I., Van Zeeland M.A., Heidbrink W.W. and Austin M.E. 2019 Central ion cyclotron emission in the DIII-D tokamak *Nucl. Fusion* **59** 086011
- [70] Shestakov Y.V., Nikolenko D.M., Rachek I.A., Toporkov D.K. and Yurchenko A.V. 2019 Nuclear-Polarized Hydrogen/Deuterium Molecular Source *Phys. Part. Nucl.* **50** 513
- [71] Engels R. et al 2020 Production of HD Molecules in Definite Hyperfine Substates *Phys. Rev. Lett.* **124** 113003

- [72] Bortolon A. *et al* 2016 High frequency pacing of edge localized modes by injection of lithium granules in DIII-D H-mode discharges *Nucl. Fusion* **56** 056008
- [73] Agram A., Bouffard V., Roinel Y. and Roubeau P. 1980 A new polarized target material: 6LiD *J. Phys. Lett.* **41** 309
- [74] Bouffard V., Roinel Y., Roubeau P. and Agram A. 1980 Dynamic nuclear polarization in 6LiD *J. Phys.* **41** 1447
- [75] Wei X. *et al* 2013 Boosting Deuteron Polarization in HD Targets: Experience of moving spins between H and D with RF methods during the E06-101 experiment at Jefferson Lab *XVth Int. Workshop on Polarized Sources, Targets, and Polarimetry, Proc. Sci. (Charlottesville, VA, USA, 9–13 September 2013)* vol 16 (available at: <https://pos.sissa.it/182/016/pdf>)
- [76] Chen W.C., Gentile T.R., Ye Q., Walker T.G. and Babcock E. 2014 On the limits of spin-exchange optical pumping of ^3He *J. Appl. Phys.* **116** 014903
- [77] Jacob R.E., Morgan S.W., Saam B. and Leawoods J.C. 2001 Wall Relaxation of ^3He in Spin-Exchange Cells *Phys. Rev. Lett.* **87** 143004
- [78] Farrell M., Hoppe M. and Schoff M. 2015 private communication (General Atomics)
- [79] Tafti S. 2020 *Magnetic Resonance Imaging of Spin-Polarized ^3He and ^{129}Xe* University of Virginia Thesis (<https://doi.org/10.18130/v3-h4e5-4t97>)
- [80] Tafti S., Liu J., Deur A., Sandorfi A.M., Wei K., Wei X., Zheng X. and Miller G.W. 2023 Encapsulation of spin-polarized ^3He in tokamak fusion pellets *Nat. Phys.* (submitted)
- [81] Tobias W.A., Cates G.D., Chaput J., Deur A., Rohrbach S. and Singh J. 2003 Application of sol-gel technology to high pressure polarized ^3He nuclear targets 2002 *Proc. Testing QCD through Spin Observables in Nuclear Targets (Charlottesville, VA, USA, 18-20 April 2002)* (World Scientific) p 213
- [82] Reynolds H., Baxamusa S., Haan S.W., Fitzsimmons P., Carlson L., Farrell M., Nikroo A. and Watson B.J. 2016 Surface oxygen micropatterns on glow discharge polymer targets by photo irradiation *J. Appl. Phys.* **119** 085305
- [83] Zheng X. *et al* 2004 Precision measurement of the neutron spin asymmetries and spin-dependent structure functions in the valence quark region *Phys. Rev. C* **70** 065207
- [84] Hollmann E.M. 2022 private communication (University California San Diego)
- [85] Parks P.B. and Turnbull R.J. 1978 Effect of transonic flow in the ablation cloud on the lifetime of a solid hydrogen pellet in a plasma *Phys. Fluids* **21** 1735
- [86] Parks P.B. and Baylor L.R. 2005 Effect of Parallel Flows and Toroidicity on Cross-Field Transport of Pellet Ablation Matter in Tokamak Plasmas *Phys. Rev. Lett.* **94** 125002
- [87] Burrell K.H. *et al* 2005 Advances in understanding quiescent H-mode plasmas in DIII-D *Phys. Plasmas* **12** 056121
- [88] Chen X., Fisher R.K., Pace D.C., Garcia-Munoz M., Chavez J.A., Heidbrink W.W. and Van Zeeland M.A. 2012 Near midplane scintillator-based fast ion loss detector on DIII-D *Rev. Sci. Instrum.* **83** 10D707
- [89] Duong H.H. and Heidbrink W.W. 1993 Confinement of fusion produced MeV ions in the DIII-D tokamak *Nucl. Fusion* **33** 211
- [90] Zweben S.J., Kornack T.W., Majeski D., Schilling G., Skinner C.H., Wilson R. and Kuzma N. 2003 Evaluation of possible nuclear magnetic resonance diagnostic techniques for tokamak experiments *Rev. Sci. Instrum.* **74** 1460
- [91] Pfeiffer W.W., Davidson R.H., Miller R.L. and Waltz R.E. 1980 ONETWO: a computer code for modeling plasma transport in tokamaks *General Atomics Report GA-16178* (<https://doi.org/10.2172/6861782>)
- [92] St. John H., Taylor T.S., Lin-Liu Y.R. and Turnbull A.D. 1995 Transport simulation of negative magnetic shear discharges *Proc. 15th Int. Conf. on Plasma Physics and Controlled Nuclear Fusion Research (IAEA-CN-60/D-P22) (Seville, Spain Sept 26 - Oct 1, 1994)* vol 3 p 603 (available at: www-naweb.iaea.org/naweb/physics/FEC/STIPUB948_VOL3.pdf)
- [93] Burrell K.H., Austin M.E., Greenfield C.M., Lao L.L., Rice B.W., Staebler G.M. and Stallard B.W. 1998 Effects of $E \times B$ velocity shear and magnetic shear in the formation of core transport barriers in the DIII-D tokamak *Plasma Phys. Control. Fusion* **40** 1585
- [94] Chrystal C., Burrell K.H., Grierson B.A., Haskey S.R., Groebner R.J., Kaplan D.H. and Briesemeister A. 2016 Improved edge charge exchange recombination spectroscopy in DIII-D *Rev. Sci. Instrum.* **87** 11E512
- [95] Wade M.R. *et al* 1995 Helium transport and exhaust studies in enhanced confinement regimes in DIII-D *Phys. Plasmas* **2** 2357
- [96] Haskey S.R., Stagner L., Grierson B.A., Chrystal C., DeGrandchamp G.H., Heidbrink W.W., Van Zeeland M.A. and Vincena S. 2021 Radially resolved active charge exchange measurements of the hydrogenic isotope fraction on DIII-D *Rev. Sci. Instrum.* **92** 043535
- [97] Heidbrink W.W., Chrien R.E. and Strachan J.D. 1983 Burn-up of fusion-produced tritons and ^3He ions in PLT and PDX *Nucl. Fusion* **23** 917
- [98] Scott L.A., Schneggenburger R.G. and Anderson P R 1986 Deuterium permeation properties of beta-irradiated and unirradiated poly(vinyl alcohol) and polystyrene shells *J. Vac. Sci. Technol. A* **4** 1155
- [99] Tsai F.Y., Blanton T.N., Harding D.R. and Chen S.H. 2003 Temperature dependence of the properties of vapor-deposited polyimide *J. Appl. Phys.* **93** 3760
- [100] Prasad M.K., Estabrook K.G., Harte J.A., Craxton R.S., Bosch R.A., Busch Gar. E. and Kollin J.S. 1992 Holographic interferograms from laser fusion code simulations *Phys. Fluids B* **4** 1569
- [101] Craxton R.S. (ed) 1995 Self-interference patterns and their application to target characterization *LLE Review* 64 p 175
- [102] Rakitzis T.P., Samartzis P.C., Toomes R.L., Kitsopoulos T N, Brown A, Balint-Kurti G.G., Vasyutinskii O.S. and Beswick J.A. 2003 Spin-Polarized Hydrogen Atoms from Molecular Photodissociation *Science* **300** 1936
- [103] Rakitzis T.P. 2005 Highly Spin-Polarized Atoms and Molecules from Rotationally State-Selected Molecules *Phys. Rev. Lett.* **94** 083005
- [104] Rubio-Lago L., Sofikitis D., Koubenakis A. and Rakitzis T.P. 2006 Time-dependent polarization transfer from molecular rotation to nuclear spin *Phys. Rev. A* **74** 042503
- [105] Sofikitis D., Glodic P., Koumarianou G., Jiang H., Bougas L., Samartzis P.C., Andreev A. and Rakitzis T.P. 2017 Highly Nuclear-Spin-Polarized Deuterium Atoms from the UV Photodissociation of Deuterium Iodide *Phys. Rev. Lett.* **118** 233401
- [106] Kannis C.S., Suarez J. and Rakitzis T.P. 2022 Macroscopic production of spin-polarised hydrogen atoms from the IR-excitation and photodissociation of molecular beams *Mol. Phys.* **120** e1975053
- [107] Kannis C.S. and Rakitzis T.P. 2021 Macroscopic production of highly nuclear-spin-polarized molecules from IR-excitation and photodissociation of molecular beams *Chem. Phys. Lett.* **784** 139092
- [108] Rakitzis T P 2022 private communication (University of Crete)
- [109] Bernstein M.A., King K.F. and Zhou X.J. 2004 *Handbook of MRI Pulse Sequences* (Burlington, MA: Elsevier Academic Press) (<https://doi.org/10.1016/B978-0-12-092861-3.X5000-6>)
- [110] Zheng Y., Cates G.D., Mugler J.P. III, Tobias W.A. and Miller G.W. 2014 Very-low-field MRI of laser polarized xenon-129 *J. Magn. Reson.* **249** 108